Strong Lensing analysis of SPT-CL J2325−4111 and SPT-CL J0049−2440, two Powerful Cosmic Telescopes ($R_E > 40''$) from the SPT Clusters Sample

Guillaume Mahler [ID],[1,2,3] Keren Sharon [ID],[4] Matthew Bayliss [ID],[5] Lindsey. E. Bleem [ID],[6,7,8] Mark Brodwin [ID],[9] Benjamin Floyd [ID],[10] Raven Gassis,[11] Michael D. Gladders [ID],[7,8] Gourav Khullar [ID],[12] Juan D. Remolina González [ID],[4] and Arnab Sarkar [ID][13]

[1]*STAR Institute, Quartier Agora - Allée du six Août, 19c B-4000 Liège, Belgium*
[2]*Centre for Extragalactic Astronomy, Durham University, South Road, Durham DH1 3LE, UK*
[3]*Institute for Computational Cosmology, Durham University, South Road, Durham DH1 3LE, UK*
[4]*Department of Astronomy, University of Michigan, 1085 S. University Ave, Ann Arbor, MI 48109, USA*
[5]*Department of Physics, University of Cincinnati, Cincinnati, OH 45221, USA*
[6]*Argonne National Laboratory, High-Energy Physics Division, Argonne, IL 60439*
[7]*Kavli Institute for Cosmological Physics, University of Chicago, 5640 South Ellis Avenue, Chicago, IL 60637, USA*
[8]*Department of Astronomy and Astrophysics, University of Chicago, 5640 South Ellis Avenue, Chicago, IL 60637, USA*
[9]*Department of Physics and Astronomy, University of Missouri, 5110 Rockhill Road, Kansas City, MO 64110, USA*
[10]*Faculty of Physics and Astronomy, University of Missouri-Kansas City, 5110 Rockhill Road, Kansas City, MO 64110, USA*
[11]*Department of Physics, University of Cincinnati*
[12]*Department of Physics and Astronomy and PITT PACC, University of Pittsburgh, Pittsburgh, PA 15260, USA*
[13]*MIT Kavli Institute for Astrophysics and Space Research, 70 Vassar St, Cambridge, MA 02139, USA*

ABSTRACT

We report the results from a study of two massive ($M_{500c} > 6.0 \times 10^{14} M_\odot$) strong lensing clusters selected from the South Pole Telescope cluster survey for their high Einstein radius ($R_E > 40''$), SPT-CL J2325−4111 and SPT-CL J0049−2440. Ground-based and shallow HST imaging indicated extensive strong lensing evidence in these fields, with giant arcs spanning $18''$ and $31''$, respectively, motivating further space-based imaging followup. Here, we present multiband HST imaging and ground-based Magellan spectroscopy of the fields, from which we compile detailed strong lensing models. The lens models of SPT-CL J2325−4111 and SPT-CL J0049−2440 were optimized using 9, and 8 secure multiple-imaged systems with a final image-plane rms of $0\rlap{.}''63$ and $0\rlap{.}''73$, respectively. From the lensing analysis, we measure the projected mass density within 500 kpc of $M(< 500\ \mathrm{kpc}) = 7.30 \pm 0.07 \times 10^{14} M_\odot$, and $M(< 500\ \mathrm{kpc}) = 7.12^{+0.16}_{-0.19} \times 10^{14} M_\odot$ for these two clusters, and a sub-halos mass ratio of 0.12 ± 0.01 and $0.21^{+0.07}_{-0.05}$, respectively. Both clusters produce a large area with high magnification ($\mu \geq 3$) for a source at $z = 9$, $\mathcal{A}^{lens}_{|\mu|\geq3} = 4.93^{+0.03}_{-0.04}$ arcmin^2, and $\mathcal{A}^{lens}_{|\mu|\geq3} = 3.64^{+0.14}_{-0.10}$ arcmin^2 respectively, placing them in the top tier of strong lensing clusters. We conclude that these clusters are spectacular sightlines for further observations that will reduce the systematic uncertainties due to cosmic variance. This paper provides the community with two additional well-calibrated cosmic telescopes, as strong as the Frontier Fields, suitable for studies of the highly magnified background Universe.

Keywords: Galaxy clusters (584) — Gravitational lensing (670) — Strong gravitational lensing (1643) — Dark matter distribution (356) — SPT-CL J2325−4111 — SPT-CL J0049−2440 — SPT-CL J0512−3848

1. INTRODUCTION

Corresponding author: Guillaume Mahler
guillaume.mahler@uliege.be

Clusters of galaxies are located at the nodes of the cosmic web and represent the largest structures of dark matter. Their mass distribution present a remarkable self-similarity in the outskirts (McDonald et al. 2017). However, the densest region located at the core of the structure deviates from this scale-free distribution. This

region is prone to ongoing merging activity, where both luminous and dark matter co-evolve. While luminous matter is commonly observed, dark matter remain elusive, and only probed indirectly. Fortunately, the densest regions of cluster cores produce strong gravitational lensing, offering constraining power to map the underlying matter distribution regardless of its nature and provide a magnified view of the distant Universe.

Past studies have used strong lensing clusters to study a large breadth of topics, often even in one sight-line. Frequently addressed questions focus on: the detailed mapping of the cluster underlying matter distribution, estimating both visible and dark contributions (e.g., Jauzac et al. 2014; Furtak et al. 2023); tests of cold dark matter (CDM) alternative candidates (Natarajan et al. 2017; Harvey et al. 2017; Robertson et al. 2019; Sirks et al. 2022); comparisons of galaxy-galaxy lenses occurrences in the dense environments of clusters to simulations (Robertson 2021a; Meneghetti et al. 2022a); detection of filamentary structure, connecting cluster halos to the cosmic web (e.g., Jauzac et al. 2012; Tam et al. 2022); constraints on the galaxy halo/sub-halo mass ratio (Mahler et al. 2019) and sub-halo mass function (e.g., Natarajan et al. 2017; Sirks et al. 2022); constraining lensing mass clumpiness, producing microlensing from stars and primordial black holes (e.g., Kelly et al. 2018; Diego et al. 2018; Mahler et al. 2023a); measuring spatially-resolved properties of giant arcs, such as winds (Fischer et al. 2019), sizes of star forming clumps (Johnson et al. 2017; Claeyssens et al. 2023), metallicity gradients and kinematics (Patrício et al. 2018), and leaking ionizing photon radiation (Rivera-Thorsen et al. 2019) at tens of parsec resolution at $z > 1$; using caustic crossing events to probe stars at the dawn of the universe (e.g., Welch et al. 2022; Hsiao et al. 2023; Adamo et al. 2024); detecting magnified high-redshift galaxies, probing the intrinsically fainter galaxies more representative of early populations (Atek et al. 2024) and offering constraints on the faint end of the high-z luminosity function (Atek et al. 2015; Bouwens et al. 2017; Livermore et al. 2017; de La Vieuville et al. 2019); constraining cosmological parameters such as the dark energy equation of state parameter (w) and Ω_M (e.g., Jullo et al. 2010; Acebron et al. 2017), and time-delay measurements of H_0 (e.g., Grillo et al. 2018; Napier et al. 2023).

Owing to their diverse core properties (McDonald et al. 2017), clusters with the same total mass may not exhibit similar strong lensing cross section. To identify strong-lensing lines of sight requires selection based properties beyond their total mass. Two main methods of discovery are employed to find lines of sight of lensing clusters: lensing-selected and non-lensing selected.

Lensing-selected surveys have traditionally searched for substantial lensing evidence, typically in the form of highly magnified giant arcs by inspection of large data sets of shallow ground-based data. Utilising the SDSS data and catalogs resulted with numerous lenses (e.g., Bayliss et al. 2011a,b; Stark et al. 2013; Dahle et al. 2015; Johnson et al. 2017; Sharon et al. 2020) mainly at low arc and lens redshifts. More recently, imaging from the Dark Energy Survey yielded strong lensing samples based on visual inspection (e.g., Diehl et al. 2017; Khullar et al. 2021) or machine-assisted identification (e.g., Huang et al. 2021).

Non-lensing based approaches commonly rely on deep or high-resolution optical imaging followup of cluster samples that were selected as likely lenses based on other criteria, usually high total mass as indicated from X-ray, sub-mm, or optical mass proxies. Examples of such surveys include the Hubble Space Telescope (HST) followup of the MAssive Cluster Survey (MACS; Ebeling et al. 2001), the optical ground-based and HST followup of the South Pole Telescope cluster sample (Bleem et al. 2015, 2020), the Local Cluster Substructure Survey (LoCuSS; Smith et al. 2005) followup of X-ray selected clusters, HST followup of sub-mm selected lens candidates (dusty GEM; Cañameras et al. 2015), and spectroscopic followup of X-ray selected clusters with VLT/MUSE (e.g. KALEIDOSCOPE cluster survey P.ID: 0102.A-0718(A), PI: A. Edge; Patel et al. 2024). Several treasury programs with HST employed a hybrid selection approach where lensing-evidence from shallower or low resolution imaging were combined with total mass criteria to increase the sample, e.g. CLASH (25 clusters, Postman et al. 2012), and RELICS (41 clusters, Coe et al. 2019).

To fully benefit from the lines of sight of strong gravitational lenses requires space-based observations, such as with HST or JWST, and relatively shallow HST follow-up of the aforementioned samples resulted with numerous discoveries as listed at the beginning of the introduction. However, the high investment of space-based telescope time is reserved for a few, extraordinary lenses, carefully picked as the best lenses coming out of the previous surveys. Such are the Frontiers Fields (Lotz et al. 2017), for which the original program used 840 HST orbits to observe six strong lensing clusters. More recently, studies of cluster-lensed galaxies using JWST (e.g., TEMPLATES, Rigby et al. 2023; UNCOVER, Bezanson et al. 2022; PEARLS, Windhorst et al. 2023; SMACSJ0723, Mahler et al. 2023b; Caminha et al. 2022; Golubchik et al. 2022; SPT0615, Adamo et al. 2024; WHL0137, Welch et al. 2022) have pushed the limits of redshift, luminosity, and resolution.

While tremendous discoveries were enabled even in single well-studied lines of sight (e.g., UNCOVER Bezanson et al. 2022), both the HST and JWST analyses caution that cosmic variance might play an important role in our ability to infer the properties of high redshift populations of galaxies. Salmon et al. (2020) identified 322 new candidates at $z > 6$ behind the 41 clusters uniformly observed by HST as part of RELICS, reporting a large field-to-field variance, where in some fields no galaxy candidates above z>5.5 were found (Mahler et al. 2019). A recent JWST analysis (Chemerynska et al. 2024) reported a potential overabundance of UV galaxies behind the lensing cluster Abell 2744. Identifying more clusters that are on par with the lensing power of the Frontier-Fields clusters will open up an important discovery space.

This paper presents two new exquisite well-calibrated strong lensing sight-lines with obvious untapped discovery potential coming at the end of a dedicated search based from SPT optical follow-up using the PISCO imager and HST-SNAP follow-up. These targets, SPT-CL J2325−4111 and SPT-CL J0049−2440, are two of the most promising strong lensing clusters from the SPT cluster sample.

The SPT cluster sample is based on the detection and calibration of the Sunyaev Zel'dovich effect observed in the CMB radiation (Bleem et al. 2015, 2020 and references therein). The entire cluster sample was followed up with multi-band imaging using Magellan/PISCO (Bleem et al. 2020; Stalder et al. 2014), facilitating the identification of strong lensing candidates, among other cluster science (e.g. Somboonpanyakul et al. 2021), extensive spectroscopic campaigns using Magellan and Gemini (Bayliss et al. 2016). Some clusters were the target of HST programs mainly for weak lensing calibration (e.g., Schrabback et al. 2021) and HST/SNAP programs provided shallow high resolution imaging (Gladders et al. 2019).

SPT-CL J2325−4111 was reported on by Bleem et al. (2015, 2020) as a $\xi = 12.5$ significance SZ detection [1], with ground-based spectroscopic redshift of $z = 0.358$ (Ruel et al. 2014). Bocquet et al. (2019) report $M_{500c} = 6.70^{+0.95}_{-1.17} \times 10^{14} h_{70}^{-1} M_\odot$ from the weak-lensing calibrated SZ signal. It was flagged as a strong lensing cluster in Table 4 of Bleem et al. (2015).

SPT-CL J0049−2440 was reported on by Bleem et al. (2020) from an analysis of the SPTPol Extended Cluster

---

Survey as a $\xi = 7.44$ significance SZ detection, with ground-based spectroscopic redshift of $z = 0.527$ (de Propris et al. 1999). Bleem et al. (2020) report $M_{500c} = 6.59^{+0.86}_{-0.98} \times 10^{14} h_{70}^{-1} M_\odot$ from the weak-lensing calibrated SZ signal. The same paper highlights this cluster as a prominent strong lens, first reported on by de Propris et al. (1999).

In this paper, we used multiband HST imaging and ground-based spectroscopy to identify lensing evidence, compute lens models, and calculate lens properties such as mass distribution, magnification, and lensing strength, showing that these clusters are excellent new strong lenses. This paper is organized as follows. We present the data used in this work in Section 2, and the lens modelling analysis in Section 3. In Section 4 we discuss the mass distribution and lensing power of those cluster, and highlight prominent lensed sources. We conclude in Section 5. We also report in Appendix B the HST imaging and spectroscopic followup of a third cluster from the same program, SPT-CL J0512−3848, which did not pan out as a similarly powerful cosmic telescope.

We assume flat ΛCDM cosmology with $\Omega_\Lambda = 0.7$, $\Omega_m = 0.3$, and $H_0 = 70$ km s^{-1} Mpc^{-1}. Magnitudes are reported in the AB system (Oke 1974).

2. DATA AND LENSING EVIDENCE

2.1. *Hubble Space Telescope*

The fields studied in this paper were observed by HST as part of Cycle 27 GO-15937 (PI: G. Mahler). Each cluster was observed with four filters, using 3 orbits of HST: one orbit with the ACS/F606W filter, one orbit with the ACS/F814W filter, and one orbit with WFC3-IR split between two filters, F105W and F140W. We obtained four sub-exposures per filter with small box sub-pixel dithers for point spread function (PSF) reconstruction and to cover chip gaps and artifacts such as the "IR Blobs" and "Death Star" (WFC3 Data Handbook; Rajan 2010). For the WFC3-IR observations we used a sampling interval parameter SPARS25.

Observations of SPT-CL J2325−4111 took place on Oct 22, 2019 (WFC3) and Oct 25, 2019 (ACS). The second visit was affected by a guide-star re-acquisition error, leading to a lost exposure in the F814W band, and was rescheduled by HOPR 91651 to Dec 10, 2019. The resulting imaging data have 1212 s in WFC3/F105W, 1312 s in WFC3/F140W, 2204 s in ACS/F606W, and 3477 s in ACS/F814W. The failed F814W sub-exposure was not used. Observations of SPT-CL J0049−2440 took place on Oct 23, 2019 (WFC3) and Oct 31, 2019 (ACS), and consists of 1212 s each in WFC3-IR/F105W and F140W, 2124 s in ACS/F606W, and 2184 s in ACS/F814W.

Data reduction was done similarly to Sharon et al. (2020). We combined all the usable sub-exposures of each filter with the AstroDrizzle package (Gonzaga et al. 2012) with a pixel scale of $0\rlap{.}''03$ pixel^{-1}, and drop size of 1.0 for the ACS images and 0.8 for WFC3. Observations that were executed over multiple visits were aligned to a common world coordinate system (WCS) using `tweakreg`, and the WCS solutions were applied back to the individual sub-exposures with `tweakback`. Finally, we drizzled all the images of each field onto the same pixel frame using the same parameters as above. The clusters are presented in Figure 1 and Figure 2.

2.2. *Lensing Evidence*

Multiple images (arcs) of background galaxies are used as strong lensing evidence to constrain the lens model of each cluster. We identified multiple images of each background source through visual inspection of the HST imaging, based on color and morphology of the images. We have obtained spectroscopic confirmation of a subset of those (see Section 2.3 below). Figures 1 and 2 show the identified multiple images in each field over-plotted on the HST data (see also Figure 9 for zoom-ins of all multiply-imaged systems identified). The multiple images of each source are labeled and color-coded by source ID. The coordinates, spectroscopic redshift information and other notes specific to each system are listed in Table 2. In some of these sources we further identified emission clumps or other substructure, that could be matched between images, and used as additional constraints in the lens models. The IDs of images of lensed galaxies are labeled as A.B(.C) where A indicates the source ID (or system name); B identifies the lensed image within the multiple images family; C is the ID of emission knot within the image if we used more than one substructure of the images as constraint. For example, ID 1.3.2 would identify the third multiple image of knot #2 in Source 1.

In SPT-CL J2325−4111 we identified a total of 9 secure strongly-lensed sources with multiple images. Of these, four strongly-lensed sources are spectroscopically confirmed. In the field of SPT-CL J0049−2440 we identified a total of 8 secure systems, with spectroscopic redshifts for two. Other arc-like features that were not used in this analysis can be seen in the HST images. We further discuss the lensing evidence in Section 3.2

2.3. *Spectroscopy*

Spectroscopic observations of SPT-CL J2325−4111 and SPT-CL J0049−2440 were obtained as part of larger campaigns to follow up SPT-selected clusters of galaxies. We collected all the available spectroscopy for these two clusters for the primary purpose of measuring spectroscopic redshifts of candidate lensed sources and cluster-member galaxies. These observations used the Magellan 6.5-m telescopes at Las Campanas Observatory, with the Inamori-Magellan Areal Camera and Spectrograph (IMACS; Dressler et al. 2011) on Magellan I-Baade, the upgraded Low Dispersion Survey Spectrograph (LDSS3-C) on Magellan II-Clay, and the Folded port InfraRed Echellette (FIRE; Simcoe et al. 2013) spectrograph on Magellan I-Baade. We describe the observations and data reduction of Magellan LDSS3, IMACS, and FIRE in the following subsections. Spectroscopy results for specific objects in the following subsection refer to the object IDs in Figure 1, Figure 2, and Table 2. The compilation of spectroscopic catalogs for these fields is described in Section 2.4.

2.3.1. *Magellan LDSS3 and IMACS MOS sopectroscopy*

We obtained spectroscopy of SPT-CL J2325−4111 and SPT-CL J0049−2440 with custom designed multi object slit (MOS) masks (Remolina Gonzàlez 2021). Spectroscopic observations that took place before the HST data were in hand used Magellan/PISCO imaging to guide the mask design (see Bleem et al. 2020, for description of the PISCO data).

SPT-CL J2325−4111 was observed with LDSS3 on June 7, 2016, with two multi object slit masks, each observed for 4×25 minutes, in clear conditions and seeing of $1\rlap{.}''0$. Slits were placed on candidate lensed features as identified from ground-based imaging, including 2.1, 2.3, 3.1, 4.1, 4.3, and on cluster-member galaxies selected by color. SPT-CL J0049−2440 was observed with LDSS3 on Dec 20, 2017, with one multi object slit mask, 2×20 min exposure, in clear weather and $0\rlap{.}''8$ seeing. Slits were placed on candidate lensing features, including 1.2, 5.1/5.2, 6.1/6.2, and 4.3, and cluster-member galaxies.

SPT-CL J2325−4111 was observed with IMACS on May 27, 2015, in clear weather and seeing of $0\rlap{.}''7 - 0\rlap{.}''75$. We observed one multi object slit mask in three subexposures, for a total of 6600 s, using the `IMACS_grism_200` disperser. Only 10 out of the 108 slits were within the HST field of view, targeting arc-like features as identified from ground based data, including the giant arc of source 1 for which a spectroscopic redshift of $z = 1.5790$ was previously observed with Gemini/GMOS (Bayliss et al. 2016). The remaining slits in the large field of view of IMACS were placed primarily on cluster-member galaxies, selected by color from ground-based photometry.

We reduced the LDSS3 and IMACS spectra using the Carnegie Observatories System for Multi-Object Spec-
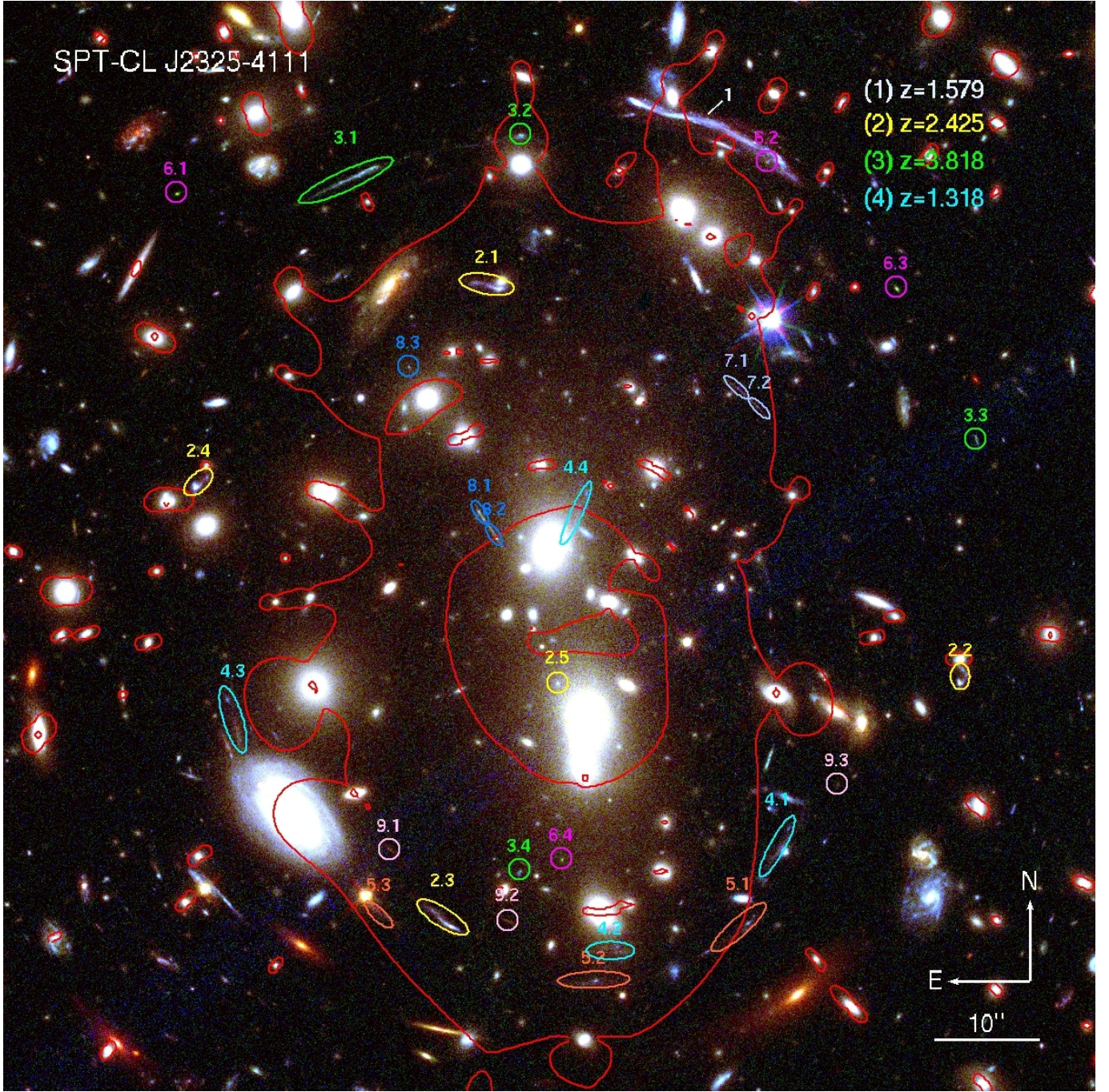
Figure 1. Composite color images of the field of SPT-CL J2325−4111, from HST imaging in WFC3IR/F140W (red), ACS/F814W (green), and ACS/F606W (blue). Multiple images of lensed features are labeled and color-coded by the source ID. The coordinates, redshifts (where available), and references of these strong lensing systems are presented in Table 2. The critical curve for a source plane at $z = 2$ is shown in solid red. North is up and East is to the left.

Figure 2. Composite color images of the field of SPT-CL J0049−2440, from HST imaging in WFC3IR/F140W (red), ACS/F814W (green), and ACS/F606W (blue). Multiple images of lensed features are labeled and color-coded by the source ID. The coordinates, redshifts (where available), and references of these strong lensing systems are presented in Table 2. The critical curve for a source plane at $z = 2$ is shown in solid red. North is up and East is to the left.
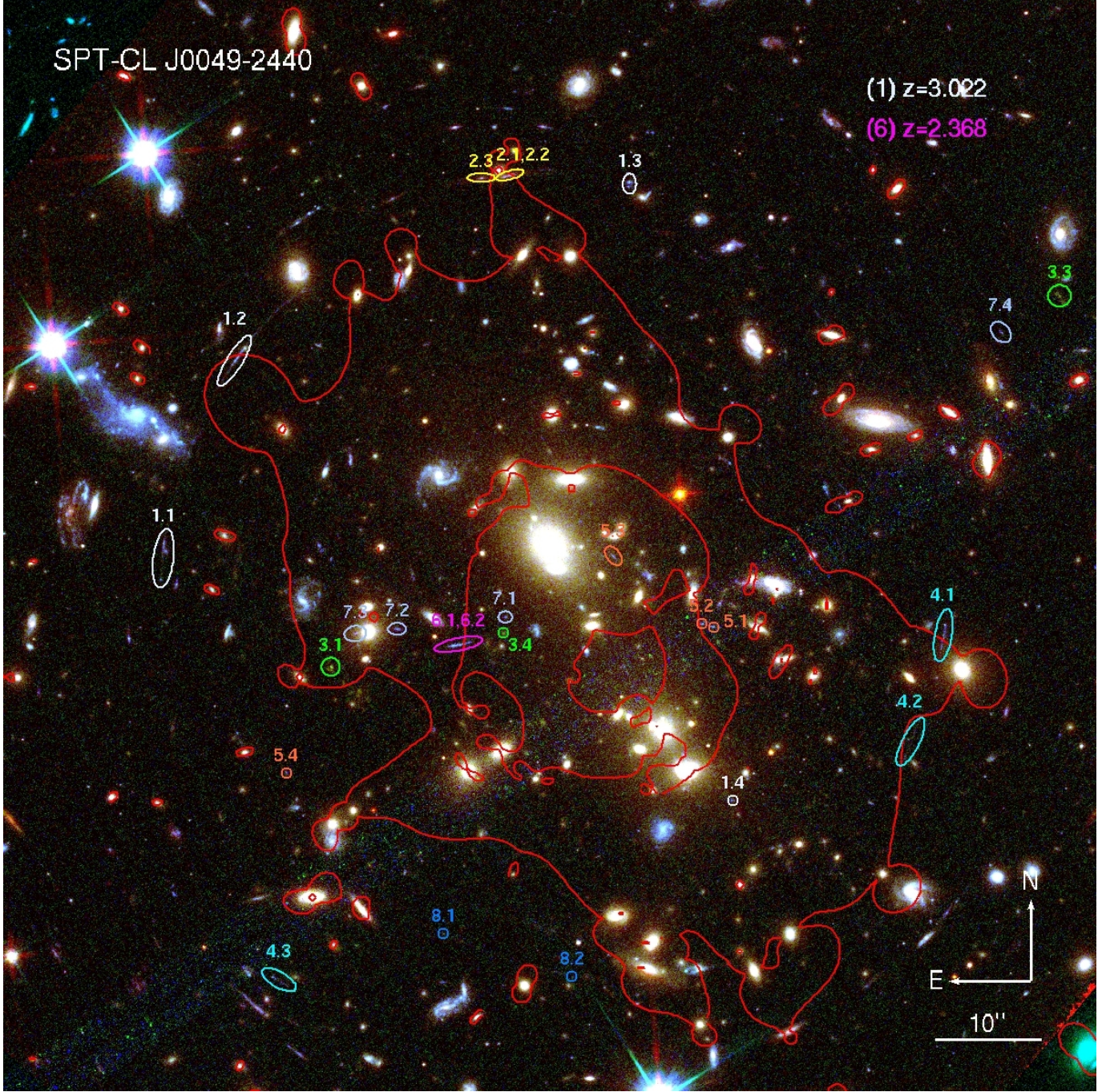
troscopy (COSMOS[2]; Dressler et al. 2011; Oemler et al. 2017). The de-biased raw data were flat-fielded using flat field images that were taken immediately before or after each science frame. For wavelength calibration, we used HeNeAr comparison arc frames, also taken immediately before or after each science observation. Sub-exposures of the same mask were coadded, and the off-source area within the same slit was used to subtract the sky. The 1-D spectrum of each targeted object was extracted using custom Python routines following standard methods.

While yielding ample redshifts for cluster member galaxies and foreground objects, both LDSS3 and IMACS resulted with limited success in securing spectroscopic redshifts of lensed galaxies. This was in part because these observations took place prior to our HST program and many arcs were not identified at the time, and in part due to the wavelength coverage of these instruments.

2.3.2. *Magellan FIRE spectroscopy of arc candidates*

SPT-CL J2325−4111 and SPT-CL J0049−2440 were spectroscopically observed with the FIRE spectrograph on December 4 and 5 2019, in good conditions, and seeing ranging between $0.''55 − 1.''0$. Data reduction used standard IRAF techniques, and the redshifts were measured from lines identified primarily in the 2-D spectra.

In the field of SPT-CL J2325−4111, we targeted arcs 2.3, 7.1, 8.1, and 3.1 on the first night and arcs 2.2, 4.3, 3.1 and c1 (a blue arc-like feature north of 4.1) on the second night. Each target was observed with a $1.''0$ slit for 2×602 sec unless otherwise specified, executing a small A/B dither along the slit between exposures.

We measured secure redshifts for three sources with FIRE. Source 2 is at $z = 2.4253 \pm 0.0007$, based on bright [OIII], Hα, and Hβ lines in emission in the spectrum of Arc 2.3. We identified the same lines in the spectrum of a Arc 2.2, an image of the same source, obtained on the second night. The spectrum of Arc 3.1 in night 1 was inconclusive; A deeper observation of 2×1205 sec was obtained for Arc 3.1 on the second night, resulting in a secure redshift of 3.8180 ± 0.0007 from two OIII $\lambda\lambda 4959, 5007$Å lines.

We identified one line in the spectrum of Arc 4.3, which can be interpreted as either [OIII] $\lambda 5007$Å at $z = 2.037$, or Hα at $z = 1.318$. The lensing analysis strongly favored the $z = 1.318$ solution, resulting in a $5\times$ lower χ^2, and a factor of 10 reduction in source plane rms. We, therefore, adopt this solution as the redshift of this source.

No emission lines were identified in the spectra of arcs 7.1, 8.1, and c1 at the depth of our data.

In the field of SPT-CL J0049−2440, we targeted arcs 1.2, 2.1/2.2, 4.1, and 5.1/5.2, on the first night and arcs 1.2, 1.3, 3.1, and 6.1/6.2 on the second night. We secured a spectroscopic redshift of source 1 at $z = 3.022$ from OIII. In arcs 6.1/6.2, we observed a faint line at 16869Å, which could be either OIII 5008 at $z = 2.368$ or Hα at $z = 1.570$. We produced lens models for both solutions, and found that the lens model that used the lower redshift as constraint failed to produce the observed radial arc at the observed position, and generated predicted counter images for this arc that are not observed in the data. We therefore proceed with a redshift of $z = 2.368$ for this arc.

Spectra of the other targeted arcs in SPT-CL J0049−2440 did not yield emission lines. Since the spectrum of arc 1.3 did not confirm it as a counter-image of arc 1.2, we did not use it as constraint in the lens model.

2.4. *Spectroscopic Redshifts Measurement and Redshift Catalogs*

We extracted redshifts from the observed LDSS3, IMACS, and FIRE spectra as follows. We convolved the reduced 2D spectra with a 1D Gaussian profile along the wavelength axis. The Gaussian parameters were fit to a stack of spectra of a manually-selected clean part of the slit, to increase the signal-to-noise and derive robust values. The spectra are not strictly perpendicular to the slit, ignoring any higher-order distortion, we extracted the 1D spectra along a manually adjusted linear trace on the wavelength axis. The redshift assessment was performed by matching spectral features to the most common emission and absorption lines.

We assigned a confidence level to each spec-z based on the number and strength of spectral features according to the following rules:

- Confidence 3: secure redshift, with several strong spectral features.

- Confidence 2: probable redshift, relying on one emission line or several faint absorption features.

- Confidence 1: tentative redshift, relying on one spectral feature with low s/n.

We complemented our final catalog with the reported GMOS spectroscopy measurements for SPT-CL J2325−4111 from Bayliss et al. (2016). For sources that were measured by multiple instruments, we report the highest confidence measurement, where GMOS has the highest confidence, followed by FIRE, LDSS3, and

IMACS. Our final catalog for SPT-CL J2325−4111 contains 230 galaxies, of which 224 are not multiple images of lensed sources, and for SPT-CL J0049−2440 we have spectroscopic redshifts for 29 galaxies in the field, and redshifts of two additional lensed sources. The non-arcs catalogs are presented in Table 3 and Table 4, and redshifts of strongly lensed galaxies with multiple images are listed in Table 2. The redshift histograms for both cluster fields are presented in Figure 3.

3. STRONG LENSING ANALYSIS

3.1. *Lens Modeling*

The strong lens models were constructed using the public lens modeling software Lenstool (Jullo et al. 2007). The algorithm uses Markov Chain Monte Carlo (MCMC) sampling to determine the best-fit model, and explores the parameter space to facilitate a statistical assessment of the uncertainties in model parameters and measurements derived from the lens model. The best solution is determined by minimizing the scatter between observed and model-predicted image-plane positions of the lensing constraints, i.e., images of lensed background galaxies.

As with many other parametric algorithms, Lenstool assumes that the mass distribution of the lens can be fairly described by a linear combination of halos described by a parameterized mass distribution. Several mass density profiles are implemented, e.g., isothermal, or the Navarro–Frenk–White (NFW; Navarro et al. 1996) profile. In this work, we use the pseudo-isothermal ellipsoidal mass distribution (dPIE; Elíasdóttir et al. 2007, also referred to in the literature as PIEMD), which has an elliptical geometry, flattened core, and a truncated isothermal slope of $\rho \propto r^{-2}$. The halo is described by seven parameters: α, δ centroid, ellipticity e, position angle θ, core radius r_{core}, truncation radius r_{cut}, and normalization σ_0. Note that σ_0 represents a fiducial central velocity dispersion as defined in the dPIE parameterization, and is not equal to the observed velocity dispersion (for the parameterization of dPIE, and the relationship between an observed velocity dispersion and σ_0, we refer the reader to Elíasdóttir et al. 2007). The mass of galaxy clusters is dominated by dark matter, and may best be described by more than one dominant cluster-scale halo. Cluster-member galaxies contain a small fraction of the total cluster mass, but have an important contribution to the complexity of the lensing potential. We model cluster member galaxies as dPIE halos as well, but link their parameters more strongly to their observed stellar mass. In particular, their positional parameters (α, δ, e, θ) remain fixed to the properties of their light distribution as measured with Source

Extractor (Bertin & Arnouts 1996). The slope parameters are linked to the luminosity through scaling relations (Jullo et al. 2007) that are optimized in the modeling process for the entire galaxy catalog as a whole. Some galaxies were optimized separately from the scaling relations, including the BCGs and other galaxies in close proximity to multiple images.

The modeling process is done iteratively, starting from the most obvious and secure lensing constraints (multiple images and arcs) to inform a preliminary lens model. The model is then used to assist in identifying more images of lensed galaxies that can be used as constraints. When each new set of constraints is added to the analysis, the modeling process is re-initiated in order to not bias the model to fixate on an early solution. Table 1 lists the optimized and fixed model parameters for each cluster, with their best-fit solutions and uncertainties as determined from the MCMC analysis.

3.2. *Identification of lensing constraints*

We used the locations of multiply-imaged systems as constraints to our modelling. We identified multiple image "families" based on the morphology, color and spectroscopic redshift. When spectroscopic redshift was not available we associated the images of the family based on color and morphology only. If the spectroscopic redshift was only measured in a subset of the family we associated the same redshift to all images of the family. Table 2 lists all the identified lensed constraints; Figure 1 and Figure 2 label the multiple images of each source. The coordinates of clumps within images that were used as further constraints are only listed in the table, to avoid over-cluttering the figures. We used as constraints in our models only multiple images that were considered as secure. We consider secured candidate when morphology, color and lensing configurations through the iterative process converged toward being images of the same source. Candidate lensed system are suggestive multiply-imaged system or images within a secure system which are often too faint, or contaminated by light from a nearby galaxy, to be securely associated to lensing constraints. Although they can often be geometrically confirmed with by the lens model, we exclude them from the list of constraints in order to avoid confirmation bias (see Table 2 for systems marked with a "*c*" and considered only as candidate).

In SPT-CL J2325−4111 we identified nine multiply-imaged systems; one (system 7) is labeled as candidate and eight are considered secure. Image 6.2 is considered a candidate due to contamination from arc 1.

In SPT-CL J0049−2440 we identified nine multiply-imaged systems, all of which are secure. A candidate is
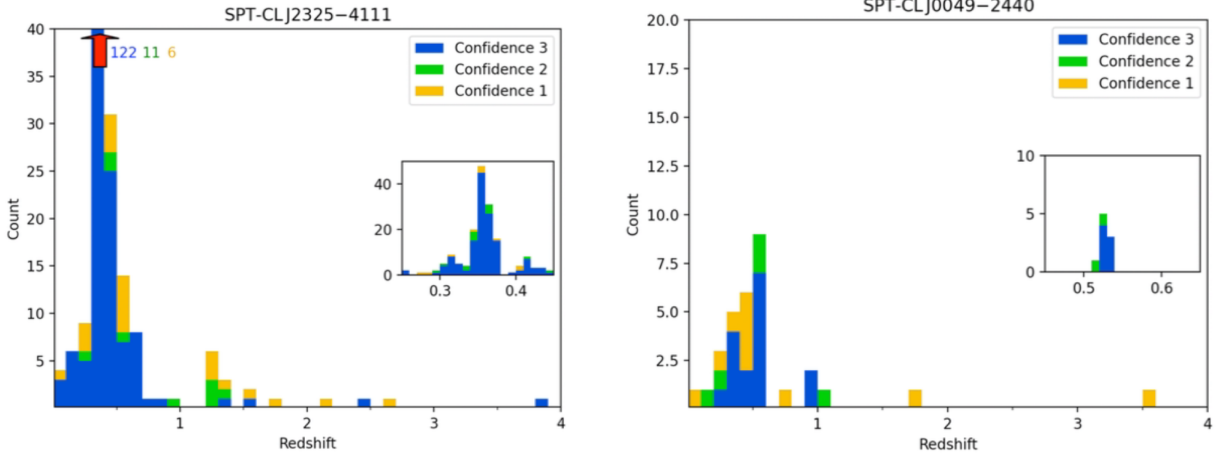
Figure 3. Redshift histogram of all the objects with spectroscopic redshift measurements in the field of view of SPT-CL J2325−4111 (left) and SPT-CL J0049−2440 (right). The redshifts are tabulated in Table 3 and Table 4, respectively. The insets show a zoom-in around each cluster redshift, to illustrate the velocity structure in a narrower redshift range. The redshift bin size is $\Delta_z =0.1$ in the main figure and $\Delta_z =0.01$ in the insets. The different colors represent the spec-z confidence level as described in Section 2.4. For better display the left histogram is cut at 40 counts and the red arrow indicates the number of galaxies in the unique redshift bin going beyond 40.

identified as image 3 of source 1. This system is further discussed in Section 4.3, and the attempt to spectroscopically confirm the candidate image is discussed in Section 2.3. Image 4.2 is an extended faint arc, likely affected by foreground galaxies. We consider it as a candidate as well.

3.2.1. *Identification of Cluster-Member Galaxies*

Cluster-member galaxies were identified based on their color with respect to the cluster red sequence (Gladders & Yee 2000) in a color-magnitude diagram, using spectroscopic redshift information where available. The catalogs were constructed as follows. We started by running Source Extractor (Bertin & Arnouts 1996) in dual image mode, using the F814W image for identification and measuring the F814W MAG_AUTO and F606W-F814W color within the same detection apertures. We flagged and removed stars and artifacts based on their location in a MU_MAX vs MAG_AUTO space. We then matched the coordinates of the photometric and spectroscopic catalogs. For SPT-CL J2325−4111, where numerous objects with spectroscopic redshifts are within the HST field of view, we fit a line to the F606W-F814W color vs. F814W magnitude of cluster members (those within $\Delta z = 0.03$ of the cluster redshift) using iterative 3σ-clipping, which successfully removes blue cluster-member galaxies from the fit. We set the red sequence selection as 5σ above and below the fit, with a faint-end limit of 25.5 mag and a bright end limit set by the magnitude of the brightest cluster galaxy (BCG), to account for intrinsic scatter in the red sequence and reduce contamination from faint field galaxies. The model

of SPT-CL J2325−4111 includes 277 cluster member galaxies, of which six were optimized separately from the scaling relations; the model of SPT-CL J0049−2440 includes 224 cluster members, two of which were optimized separately, as listed in Table 1. The color-magnitude diagrams are shown in Figure 4. Spectroscopically-confirmed cluster members, foreground, and background galaxies within the ACS field of view, are marked in color.

3.2.2. *Lens Modelling Results*

The lensing analysis of these lines of sight resulted in two well-calibrated "cosmic telescopes", as indicated by the low image plane scatter between observed and predicted images of lensed sources: rms = $0\rlap{.}''63$ for SPT-CL J2325−4111, and rms = $0\rlap{.}''73$ for SPT-CL J0049−2440.

The image plane rms reflects the ability of the best-fit lens models to describe the lensing potential and reproduce the lensing evidence. A high rms could imply that the underlying mass distribution is more complex than what is permitted by the flexibility of the parameterized modelling. On the other hand, a very low rms could point to overfitting. Our results are in the same range of other clusters with similar richness of lensing evidence in the literature (e.g. Richard et al. 2011; Zitrin et al. 2017; Cerny et al. 2018). In addition to the overall rms, we report in Table 2 an indicator of goodness of fit for each image, in the form of the distance between its observed and predicted position. These values highlight which systems and images perform better and help assess the fidelity of the model.
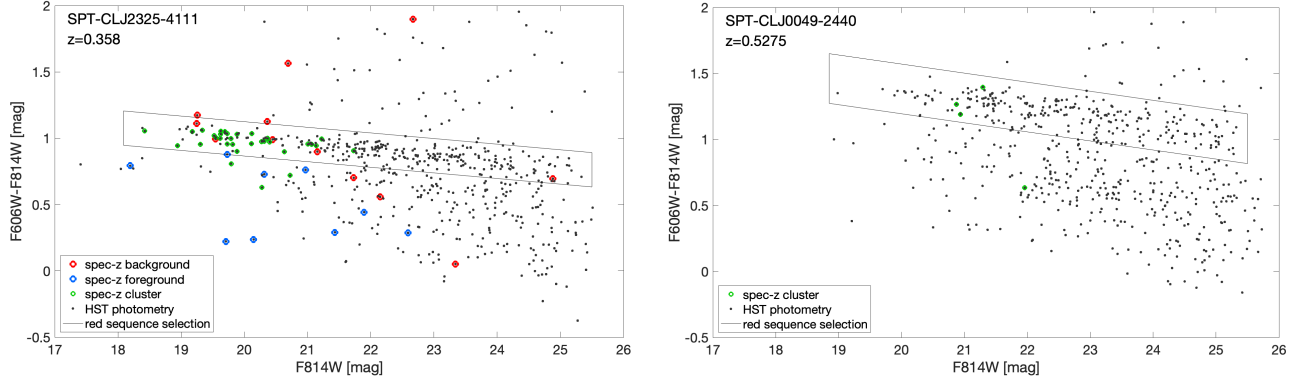
Figure 4. Color magnitude diagrams of SPT-CL J2325−4111 (left) and SPT-CL J0049−2440 (right). HST/ACS F606W-F814W color vs F814W magnitude is plotted in black for galaxies within the ACS field of view. Spectroscopically-confirmed galaxies are color-coded by their redshift with respect to the cluster (background, foreground, or at the cluster redshift, see legend). The red-sequence selection is marked with black lines. See Section 3.2.1 for more details.

Figure 1 and 2 show the critical curves for a source at $z = 2$ for the best-fit model of each cluster. We confirm the initial assessment that both of these clusters have a massive core, as indicated by the large separation between the giant arcs and the BCG. We measured the effective Einstein radius of each cluster, defined as $\theta_E = \sqrt{A/\pi}$, where A is the area of an ellipse fit to the tangential critical curve. For a source at the redshift of the most prominent giant arc in SPT-CL J2325−4111, we measured $\theta_E(z = 1.579) = 32''$, whereas for a generic $z = 9$ source plane we measured $\theta_E(z = 9) = 42''$. Similarly, for SPT-CL J0049−2440 the effective Einstein radii are $\theta_E(z = 3.022) = 36''$ and $\theta_E(z = 9) = 43''$.

The clusters are generally well-represented by one cluster-scale halo ($\sigma_0 > 1000$ km s^{-1}), with contribution from a high-mass galaxy-scale halo ($\sigma_0 \gtrsim 500$ km s^{-1}) near the cluster core, and the rest are more typical cluster-member galaxies. The best fit parameters of the lens models and their 68%-ile upper and lower limits are tabulated in Table 1. As part of the lensing analysis, the minimization process also solves for the unknown redshifts of multiply-imaged lensed sources that were used as constraints. These are reported in Table 2 as median± 68%-ile, determined directly from the MCMC sampling of the parameter space.

We also calculated the lensing magnification and the projected mass density map of each cluster. Uncertainties of these lensing outputs were derived from the MCMC sampling of the parameter space, by selecting 100 steps from the chain at random, and producing the relevant mass and magnification outputs for each of these realizations of the model. We note that the statistical uncertainties underestimate the true uncertainty and do not take into account systematic errors (see Meneghetti et al. 2017 for a detailed discussion, and

Johnson & Sharon 2016 for a quantitative assessment of systematic uncertainties as related to the number of arcs and spectroscopic redshifts).

Table 2 lists the model-predicted magnification at the observed location of each arc. For arcs without a spectroscopic redshift, the predicted magnification of each realization was calculated for the redshift parameter associated with the same step in the MCMC chain. We discuss the results in the following sections.

4. DISCUSSION

4.1. *Mass profiles and substructures*

Given the large radial extent of the lensing constraints in these lines of sight, we can accurately measure the total enclosed projected mass density out to relatively large radii. The core mass of SPT-CL J2325−4111, measured within 500 kpc, is $M(< 500 \text{ kpc}) = 7.30 \pm 0.07 \times 10^{14} \text{M}_\odot$, and the core mass of SPT-CL J0049−2440 is $M(< 500 \text{ kpc}) = 7.12^{+0.16}_{-0.19} \times 10^{14} \text{M}_\odot$.

Figure 5 shows the projected mass density profiles of SPT-CL J2325−4111 and SPT-CL J0049−2440 in the left panel, and the cumulative enclosed mass as a function of cluster-centric radius in the right panel. In both plots, the distances are measured from the BCG of each cluster. For comparison, we plot on the same figures the density profiles and cumulative mass profiles of the six Frontiers Fields clusters (Lotz et al. 2017), which we derived from the public Lenstool models of these clusters (Sharon V4[3]). We find that at projected radii beyond ∼ 200 kpc, the density profiles and cumulative enclosed mass of both clusters are comparable to the

---

[3] https://archive.stsci.edu/prepds/frontier/

Table 1. Lens Model Results and Best-Fit Parameters

Model name (Fit statistics)[e]	Component ...	α [a] ($''$)	δ [a] ($''$)	e [b]	θ [c] (deg)	σ_0 [d] (km s^{-1})	r_{cut} (kpc)	r_{core} (kpc)
SPT-CL J2325$-$4111	Halo 1 (cluster)	$7.34^{+0.28}_{-0.36}$	$11.99^{+0.94}_{-1.01}$	$0.29^{+0.01}_{-0.01}$	$73.7^{+0.6}_{-0.8}$	$1332.2^{+14.2}_{-20.1}$	[1500]	$39.9^{+0.1}_{-1.7}$
rms $= 0\rlap{.}''63$; k $= 30$	Halo 2 (galaxy)	[0.0]	[0.0]	[0.29]	[-83.04]	$619.1^{+25.8}_{-20.0}$	$21.8^{+4.5}_{-4.4}$	$4.1^{+0.5}_{-0.3}$
$\chi^2/\nu = 9.0$; dof $= 16$	Halo 3 (galaxy)	[3.40]	[16.21]	[0.31]	[77.46]	$407.1^{+6.0}_{-17.2}$	$86.0^{+17.3}_{-10.8}$	$2.0^{+0.1}_{-0.4}$
$\log(\mathcal{L}) = -54$	Halo 4 (galaxy)	[-9.04]	[47.91]	[0.16]	[-43.21]	$134.8^{+15.6}_{-14.5}$	$9.2^{+10.2}_{-13.8}$	$1.4^{+0.2}_{-1.2}$
$\log(\mathcal{E}) = -123$	Halo 5 (galaxy)	[14.95]	[30.10]	[0.13]	[22.48]	$287.4^{+8.3}_{-7.7}$	$54.1^{+6.7}_{-8.3}$	$1.2^{+0.2}_{-0.3}$
BIC $= 233$ AICc $= 221$	Halo 6 (galaxy)	[24.61]	[21.27]	[0.27]	[-18.06]	$100.2^{+25.5}_{-0.9}$	$3.4^{+4.5}_{-0.2}$	$0.9^{+1.1}_{-0.3}$
	Halo 7 (galaxy)	[35.78]	[18.15]	[0.12]	[25.57]	$19.7^{+14.9}_{-6.0}$	$37.8^{+35.9}_{-0.8}$	$2.0^{+0.4}_{-0.7}$
	L^* Galaxy	...	...	...	...	$207.6^{+12.7}_{-6.1}$	$56.8^{+13.0}_{-12.4}$	...
SPT-CL J0049$-$2440	Halo 1 (cluster)	$-7.95^{+0.87}_{-2.34}$	$-8.28^{+0.33}_{-2.22}$	$0.4^{+0.02}_{-0.09}$	$136.5^{+3.7}_{-1.5}$	$1145.5^{+49.3}_{-28.9}$	[1500]	$16.9^{+3.2}_{-1.8}$
rms $= 0\rlap{.}''73$; k $= 24$	Halo 2 (galaxy)	$1.42^{+0.41}_{-0.53}$	$-1.89^{+0.39}_{-0.5}$	$0.37^{+0.03}_{-0.03}$	$76.1^{+23.3}_{-11.3}$	$494.7^{+155.0}_{-29.0}$	$117.7^{+16.3}_{-28.8}$	$3.7^{+1.7}_{-0.6}$
$\chi^2/\nu = 19.0$; dof $= 8$	Halo 3 (galaxy)	[25.08]	[10.83]	[0.42]	[-51.14]	$267.0^{+13.5}_{-15.2}$	$10.7^{+0.7}_{-0.8}$	$0.8^{+0.4}_{-0.2}$
$\log(\mathcal{L}) = -61$	L^* Galaxy	...	...	...	...	$273.5^{+4.9}_{-19.1}$	$175.6^{+20.5}_{-28.3}$	...
$\log(\mathcal{E}) = -323$	...	...	...	...	...	...	...	...
BIC $= 215$ AICc $= 218$	...	...	...	...	...	...	...	...

NOTE—[a] α and δ are the positions measured in arcseconds relative to the reference coordinate point for SPT-CL J2325$-$4111 (R.A. = 351.298863, Decl. = -41.203566) and SPT-CL J0049$-$2440 (R.A. = 12.295750, Decl. = -24.678583). [b] Ellipticity (e) is defined as $(a^2 - b^2)/(a^2 + b^2)$, where a and b are the semi-major and semi-minor axes of the ellipse. [c] θ is measured north of east. [d] σ_0 is the normalization parameter and represents a fiducial central velocity dispersion as defined in the dPIE parameterization. Statistical uncertainties were inferred from the MCMC optimization and correspond to a 68% confidence interval. Parameters in square brackets were not optimized. The position and the ellipticities of the mass clumps associated with cluster galaxies were kept fixed according to their light distribution, and the other parameters were determined through scaling relations (see text). [e] Fit results for each model are given in the left column. rms is the scatter in the image plane; k is the number of free parameters; dof stands for the number of degrees of freedom; BIC is the Bayesian Information criterion and AICc is the corrected Akaike information criterion.

average Frontier Fields cluster. However, closer to the cluster cores (R<200 kpc), both clusters have higher mass density profiles than the Frontier Fields clusters (left panel of Figure 5). This mass distribution may provide an explanation for the high lensing efficiencey of SPT-CL J2325$-$4111 and SPT-CL J0049$-$2440, consistent with the association of clusters with higher concentration with higher lensing efficiency (Giocoli et al. 2012).

Parametric lens modeling algorithms such as `Lenstool` can separate the contribution to the lensing potential from the different mass components, to calculate the fraction of mass contained in substructures and galaxy scale halos. We estimate the substructure mass by removing Halo 1, which represents the cluster-scale dark matter halo (see Table 1), and measure the total projected mass density within 500 kpc associated with the remaining mass halos. We find that the substructure mass of SPT-CL J2325$-$4111 amounts to a fraction of 0.12 ± 0.01 of the total mass, and in SPT-CL J0049$-$2440, the substructure amounts to $0.21^{+0.07}_{-0.05}$ of the total mass (median and 68% uncertainty as de-

rived from the MCMC sampling). Previous studies reported amounts as low as 0.01 (Mahler et al. 2019) and as high as 0.3 (Mahler et al. 2020) of the total mass found in substructures. As shown in Richard et al. (2011), using a sample of 20 clusters, substructure mass ratios ranges from 0.02 to 0.78 with a median at 0.135. The strong lensing efficiency of sub-halos in the context of predictions from cosmological model (Λ-CDM) has been discussed in previous studies, see e.g., Grillo et al. (2015); Munari et al. (2016); Natarajan et al. (2017); Meneghetti et al. (2020, 2022b, 2023); Bahé (2021); Robertson (2021b); Tokayer et al. (2024) for more in-depth discussions of its impact.

4.2. Lensing Strength

Fox et al. (2022) studied the "lensing strength" of 74 strong lensing clusters with public lens models and space-based imaging data available at the time. They defined the lensing strength as the total image-plane area in which a source at $z = 9$ is magnified by a factor of 3 or above. They found that the lensing strength depends somewhat on the cluster mass, and more strongly
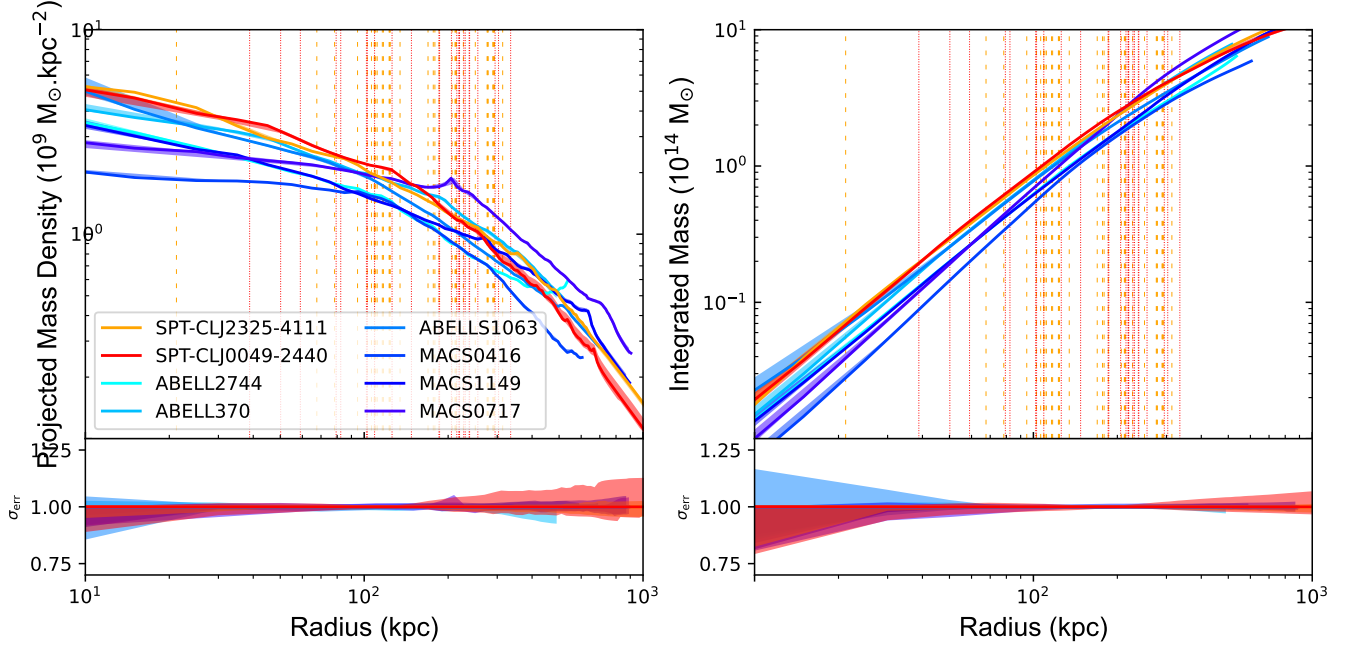
Figure 5. Projected mass density profiles (*left*) and cumulative projected mass profiles (*right*) of SPT-CL J2325−4111 (orange) and SPT-CL J0049−2440 (red) plotted against distance from the BCG. Vertical dashed orange and dotted red lines mark the position of multiple images for SPT-CL J2325−4111 and SPT-CL J0049−2440 respectively. The six Frontier Fields clusters are plotted for comparison. The mass profiles of the two clusters studied in this work have higher density than the Frontier fields in the innermost ∼ 200kpc, and comparable density and large-scale mass at larger radii.

on the inner slope of the projected mass density, where shallower inner slope can produce more powerful lenses. They also demonstrated that the Einstein radius and the projected distance between the farthest bright arc and the BCG are good predictors of lensing strength.

To contextualize the two clusters with respect to the clusters studied by Fox et al. (2022), we calculated the lensing strength of these clusters, finding $\mathcal{A}^{lens}_{|\mu|\geq3}=$ $4.93^{+0.03}_{-0.04}$ arcmin^2 for SPT-CL J2325−4111 (i.e., an area of ∼ 4.9 arcmin^2 is magnified by a factor of 3 or higher for a source at $z = 9$), and $\mathcal{A}^{lens}_{|\mu|\geq3}= 3.64^{+0.14}_{-0.10}$ arcmin^2 for SPT-CL J0049−2440. Following Fox et al. (2022), we also measured the inner slope of the mass density profile derived from the lens models, S_{50-200}, which is defined as the log of the slope of density profile measured between 50 and 200 kpc from the BCG, finding $S_{50-200} = -0.59^{-0.62}_{-0.56}$ for SPT-CL J0049−2440 and $S_{50-200} = -0.67^{-0.69}_{-0.66}$ SPT-CL J2325−4111. In Figure 6 we compare the two clusters to a large sample of strong lensing clusters from Fox et al. (2022) spanning a wide range of cluster properties, including clusters from SGAS (Sharon et al. 2020), RELICS (Coe et al. 2019), and Frontier Fields (Lotz et al. 2017). The left panel shows the $\mathcal{A}^{lens}_{|\mu|\geq3}$-$S_{50-200}$ plane, and the right panel shows the lensing strength as a function of separation between the farthest bright arc and the BCG. We find that

SPT-CL J2325−4111 and SPT-CL J0049−2440 have a higher lensing strength than most clusters with similar M_{500} or inner slope, consistent with their observed large θ_{arc} separation; they appear to have a lensing strength comparable to the Frontier Fields.

4.3. *Lensed Sources of Interest*

Each of the clusters studied in this work lenses numerous sources, which were used to constrain the lens model. While not the focus of this analysis, we highlight two prominent arcs observed in these fields. In SPT-CL J2325−4111, the image of Source 1, "J2325 Arc 1" ($z = 1.579$), appears as a bright 18″ long giant arc north of the cluster core, with observed magnitude of $m_{AB} = 19.2$ (19.1) in the F606W (F814W) band. The multiplicity of the arc was not immediately obvious: it appears that most of the arc is singly-imaged into a high-distortion arc, where only regions next to the nearby cluster member galaxy are multiple images of a small region of the source galaxy. A set of star forming clumps can be mapped with mirror symmetry about the critical curve (Figure 7). The bright core of the galaxy in the east end of the arc, as well as the long red tail to the west are singly imaged. The bottom panel of Figure 7 shows the magnification map from the best-fit lens model. We estimate a median magnification along the arc of $\mu_{med} = 10.3$; in most regions the arc is magni-
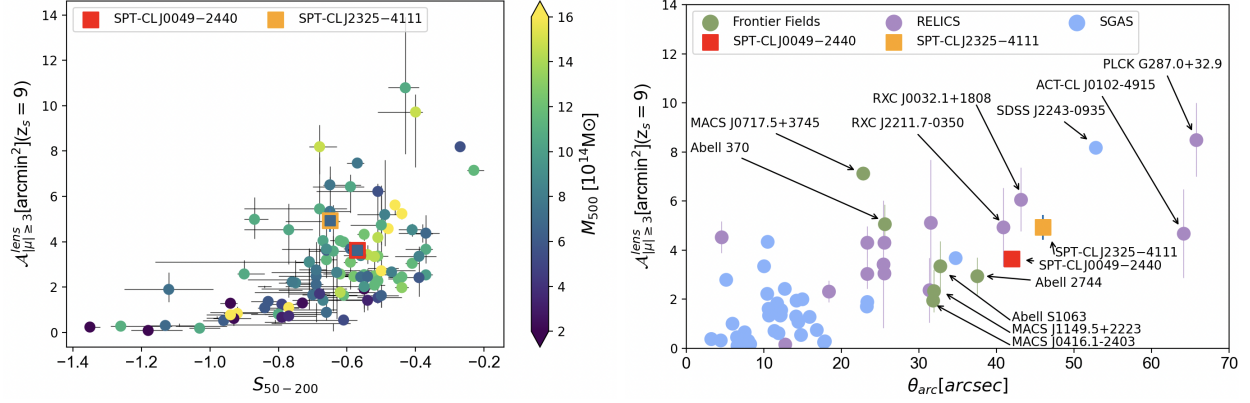
Figure 6. *Left:* Lensing strength $\mathcal{A}^{lens}_{|\mu|\geq 3}$ plotted against the central slope of the projected mass density profile (S_{50-200}). The data points are color-coded by their M_{500} mass. The comparison sample is from Fox et al. (2022) and references therein. The SPT-CL J2325−4111 and SPT-CL J0049−2440 datapoints are highlighted with orange and red edges, respectively, with their M_{500} adopted from Bocquet et al. (2019); Bleem et al. (2020). These two clusters have relatively high lensing strength compared to other clusters with similar properties. *Right:* Lensing strength plotted against the projected separation between the farthest bright arc and the BCG, compared to strong lensing cluster samples. The error bars reflect the systematic uncertainties, determined from the range of measurements obtained by different lens modeling algorithms, where available. Notably, SPT-CL J2325−4111 and SPT-CL J0049−2440 have similar lensing strengths to the Frontier Fields. Figures adapted from Fox et al. (2022).

fied by at least a factor of 8, with areas very close to the critical curve being magnified by more than 50. The brightness, prominent clumps, and indication of more details in the infrared make this arc a promising target for study by JWST.

The highly extended arc in SPT-CL J0049−2440, "J0049 Arc 1" ($z = 3.022$) spans $31''$ in the image plane. It is much fainter, and most likely comprised of two or three images along the arc. The most likely counter images (labeled 1.3 and 1.4 in Figure 2) have comparable local magnification, but do not suffer from the high distortion of the giant arc. The morphology and image-plane size of the counter images indicates that the source galaxy is quite compact; we measure a FWHM

of $0''19$ for image 1.3 using IRAF, which translates to $0.49^{+0.04}_{-0.02}$ kpc in the source plane after dividing by the square root of the lensing magnification. A separate clump, or companion galaxy, is observed nearby ($< 0''5$ in the image plane), labeled as source 1.x.2 in Table 2. Figure 7 shows a zoom-in on the faint giant arc and the lensing magnification. We estimate a median magnification of $\mu_{med} = 10.9$ along the arc. Table 2 lists the measured magnifications and their uncertainties at the positions along the arc and counter images that were used as lensing constraints. Deep, high resolution imaging with JWST could reveal substructures within this galaxy on sub-kpc scale, given its extreme tangential distortion and its large extent in the image plane.

Table 2. List of lensing constraints

ID	R.A. J2000	Decl. J2000	z_{spec} or z_{model}	Dist ($''$)	μ	Notes
SPT-CL J2325−4111 Source 1			1.5790			GMOS; Single giant arc; SL by nearby galaxy
1.1.1	351.296820	-41.187381		0.19	$8.2^{+0.1}_{-0.3}$	clump 1
1.2.1	351.295943	-41.187662		0.11	$4.4^{+0.4}_{-0.7}$	
1.1.2	351.296463	-41.187529		0.16	$24.5^{+3.1}_{-2.3}$	clump 2
1.2.2	351.296232	-41.187615		0.09	$12.7^{+3.0}_{-2.0}$	
SPT-CL J2325−4111 Source 2			2.4253			FIRE spec of 2.3, from OIII, Hβ, Hα; 2019-12-04
2.1.1	351.301880	-41.192335		0.51	$2.5^{+0.2}_{-0.2}$	clump 1
2.2.1	351.285884	-41.202655		0.31	$5.0^{+0.1}_{-0.3}$	

Table 2 *continued*
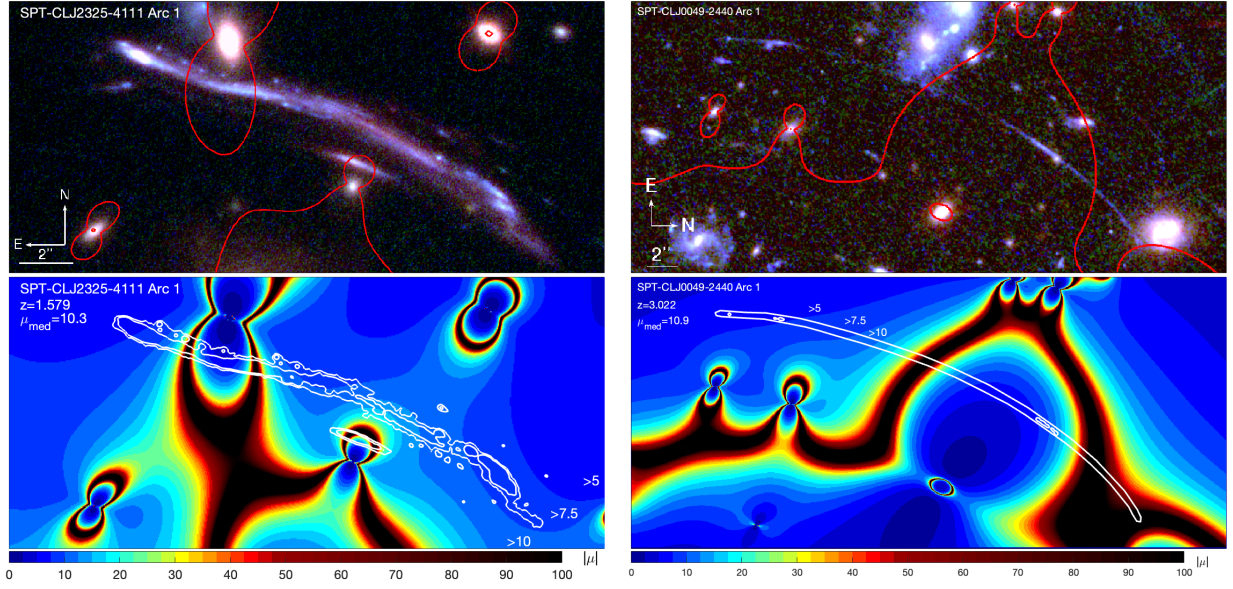
Figure 7. Zoom-in on Arc 1 in SPT-CL J2325−4111 (left) and on Arc 1 in SPT-CL J0049−2440 (right). *Top:* color composite (same data as Figure 1 and Figure 2) showing the extent of the giant arc. Critical curves for the arc redshift are overplotted in red. *Bottom:* Map of absolute magnification within the same field of view, computed from the best-fit lens model for the redshift of the arc. The colorbar at the bottom indicates the absolute magnification values. The white contours indicate the location of the giant arcs, which span a wide range of magnifications. The median magnification within the contour is 10.3 and 10.9 for SPT-CL J2325−4111 and SPT-CL J0049−2440, respectively. Note that the field of SPT-CL J0049−2440 is rotated by 90° and less zoomed-in; see compass and scale bar at the bottom left of each imaging panel for reference. Because the arc in this field is faint, the color composite was smoothed with a 3-pixel Gaussian kernel, and the external contours were placed manually to guide the eye.

Table 2 *(continued)*

ID	R.A. J2000	Decl. J2000	z_{spec} or z_{model}	Dist ($''$)	μ	Notes
2.3.1	351.303568	-41.209014		0.44	$8.4^{+0.3}_{-0.3}$	
2.4.1	351.312449	-41.197529		0.28	$25.1^{+2.7}_{-1.2}$	
2.5.1	351.299833	-41.202644		0.28	$1.4^{+0.2}_{-0.1}$	
2.1.2	351.302765	-41.192171		1.31	$7.7^{+0.7}_{-0.1}$	clump 2
2.2.2	351.285764	-41.202283		0.78	$7.6^{+0.7}_{-0.3}$	
2.3.2	351.304206	-41.208597		0.60	$10.2^{+0.5}_{-0.4}$	
2.4.2	351.312034	-41.197256		0.30	$13.1^{+0.3}_{-0.7}$	
SPT-CL J2325−4111 Source 3			3.8180			FIRE spec of 3.1, both OIII lines in K-band; 2019-12-05
3.1	351.306626	-41.189283		0.21	$42.1^{+7.2}_{-2.9}$	
3.2	351.301163	-41.188301		0.36	$5.8^{+0.6}_{-0.6}$	
3.3	351.285310	-41.196210		0.59	$4.7^{+0.2}_{-0.1}$	
3.4	351.301139	-41.207554		0.85	$3.0^{+0.1}_{-0.2}$	
SPT-CL J2325−4111 Source 4			1.3180			FIRE spec of 4.3, Hα; 2019-12-05
4.1	351.291829	-41.206459		1.03	$7.8^{+0.2}_{-0.2}$	
4.2	351.297771	-41.209536		0.56	$3.5^{+0.2}_{-0.3}$	
4.3	351.311327	-41.203079		1.19	$8.6^{+0.3}_{-0.2}$	
4.4	351.298830	-41.197679		1.03	$6.7^{+0.2}_{-0.8}$	Radial arc

Table 2 *continued*

Table 2 *(continued)*

ID	R.A. J2000	Decl. J2000	z_{spec} or z_{model}	Dist ($''$)	μ	Notes
SPT-CL J2325−4111 Source 5			1.29 ± 0.01			
5.1	351.293221	-41.208914		0.73	$9.7^{+0.3}_{-0.4}$	
5.2	351.298529	-41.210439		0.27	$8.9^{+0.4}_{-0.6}$	
5.3	351.306435	-41.208372		0.82	$13.0^{+0.4}_{-0.7}$	
SPT-CL J2325−4111 Source 6			7.02 ± 0.20			
6.1	351.313070	-41.189842		1.64	$4.9^{+0.2}_{-0.2}$	
6.2c	351.292582	-41.189019		$\cdots$	$14.4^{+1.1}_{-1.1}$	
6.3	351.288051	-41.192324		2.80	$12.0^{+0.4}_{-0.5}$	
6.4	351.299692	-41.207262		0.84	$2.1^{+0.1}_{-0.1}$	
SPT-CL J2325−4111 Source 7			$\cdots$			
7.1c	351.293554	-41.194939				Candidate system
7.2c	351.292862	-41.195442				
SPT-CL J2325−4111 Source 8			3.00 ± 0.16			
8.1	351.302596	-41.198158		0.42	$7.7^{+0.6}_{-0.7}$	Radial arc
8.2	351.301964	-41.198866		0.48	$22.5^{+7.6}_{-4.4}$	Radial arc
8.3	351.305018	-41.194379		0.04	$4.0^{+0.4}_{-1.0}$	
SPT-CL J2325−4111 Source 9			1.21 ± 0.01			
9.1	351.305663	-41.207017		0.38	$18.5^{+1.0}_{-0.7}$	
9.2	351.301553	-41.208875		0.49	$13.4^{+0.8}_{-0.5}$	
9.3	351.290113	-41.205325		0.42	$4.9^{+0.1}_{-0.2}$	
SPT-CL J0049−2440 Source 1			3.0220			FIRE spec of 1.2; OIII
1.1.1	12.306837	-24.678576	3.0220	0.32	$6.4^{+0.8}_{-0.4}$	
1.2.1	12.304789	-24.673793		0.31	$6.8^{+1.1}_{-0.8}$	
1.3.1c	12.293434	-24.669124		$\cdots$	$8.9^{+1.3}_{-0.6}$	spectroscopy attempted, not confirmed
1.4.1	12.290510	-24.685268		0.30	$2.2^{+0.5}_{-0.2}$	
1.1.2	12.306927	-24.679502		0.47	$5.7^{+0.9}_{-0.2}$	clump near Arc 1, assumed to be at the same z
1.3.2c	12.293478	-24.669244		$\cdots$	$9.8^{+1.5}_{-0.7}$	
1.4.2	12.290435	-24.685274		0.18	$2.3^{+0.5}_{-0.3}$	
SPT-CL J0049−2440 Source 2			1.52 ± 0.10			
2.1	12.296863	-24.668930		0.15	$19.9^{+4.5}_{-1.3}$	
2.2	12.297035	-24.668981		0.14	$4.3^{+1.2}_{-0.7}$	
2.3	12.297701	-24.669017		0.22	$5.0^{+0.6}_{-0.4}$	
SPT-CL J0049−2440 Source 3			3.62 ± 0.31			
3.1	12.302022	-24.681788		0.19	$5.5^{+0.7}_{-0.6}$	
3.3	12.281064	-24.672098		0.23	$2.5^{+0.2}_{-0.2}$	
3.4	12.297052	-24.680913		0.12	$3.7^{+0.6}_{-0.4}$	
SPT-CL J0049−2440 Source 4			3.03 ± 0.16			
4.1	12.284454	-24.681115		0.05	$11.7^{+0.8}_{-0.9}$	
4.2c	12.285342	-24.683749		$\cdots$	$13.9^{+2.9}_{-2.9}$	
4.3	12.303653	-24.689925		0.10	$3.9^{+0.2}_{-0.2}$	

Table 2 *continued*

Table 2 *(continued)*

ID	R.A. J2000	Decl. J2000	z_{spec} or z_{model}	Dist ($''$)	μ	Notes
SPT-CL J0049−2440 Source 5			1.37 ± 0.03			
5.1	12.291012	-24.680759		2.43	$12.8^{+0.9}_{-0.9}$	Radial arc
5.2	12.291352	-24.680671		1.98	$12.9^{+1.0}_{-0.8}$	Radial arc
5.3	12.293889	-24.678894		0.40	$9.1^{+0.8}_{-0.3}$	
5.4	12.303297	-24.684562		1.42	$3.2^{+0.2}_{-0.3}$	
SPT-CL J0049−2440 Source 6			2.368			FIRE spec of both 6.1 and 6.2; OIII
6.1	12.298507	-24.681234	2.368	0.11	71^{+70}_{-7}	Radial arc
6.2	12.298314	-24.681211	2.368	0.20	860^{+90}_{-12}	Radial arc
SPT-CL J0049−2440 Source 7			2.30 ± 0.10			
7.1	12.296999	-24.680492		0.02	$4.3^{+0.7}_{-0.4}$	
7.2	12.300114	-24.680802		0.62	$4.9^{+1.0}_{-0.4}$	
7.3	12.301315	-24.680923		0.54	$3.5^{+0.5}_{-0.3}$	
7.4	12.282750	-24.673044		0.01	$2.9^{+0.3}_{-0.1}$	
SPT-CL J0049−2440 Source 8			4.96 ± 0.61			
8.1	12.298777	-24.688750		0.10	13^{+2}_{-1}	
8.2	12.295079	-24.689882		0.08	56^{+18}_{-11}	

NOTE—The IDs, positions, and redshifts of lensed galaxies that were used as constraints in this work. Where possible, individual emission knots in each image are identified and used as lensing constraints. **The IDs of images of lensed galaxies are labeled as A.B(.C) where A is the number indicating the source ID (or system name); B is the number indicating the ID of lensed image within the multiple images family; C is a number indicating the ID of emission knot within the image if we used more than one substructure of the images as constraints. Lowercase *c* indicates a candidate arc that was not used to constrain the model. *Dist*, often called individual rmsi, is the distance in the image plane between the observed and model-predicted location of an image. The model-predicted location is calculated as the lensed coordinates of the geometric mean of source positions of all the multiple images of a given source.**

5. SUMMARY

We present strong lensing models of two clusters, SPT-CL J2325−4111 and SPT-CL J0049−2440, based on multi-band HST imaging and spectroscopic redshifts from Magellan/LDSS3, Magellan/FIRE, and Gemini/GMOS. We report the following:

- The projected mass of SPT-CL J2325−4111 within 500 kpc from the BCG is $M(< 500 \text{ kpc}) = 7.30 \pm 0.07 \times 10^{14} M_{\odot}$ (cylindrical mass), with a sub-halos mass ratio of 0.12 ± 0.01. The projected mass of SPT-CL J0049−2440 is $M(< 500 \text{ kpc}) = 7.12^{+0.16}_{-0.19} \times 10^{14} M_{\odot}$ (cylindrical mass), with a sub-halos mass ratio of $0.21^{+0.07}_{-0.05}$. A comparison of the projected mass density profiles of these clusters to those of other strong lenses indicates a higher density within the innermost few hundred kpc than that of the Frontier Fields clusters.

- The Einstein radii for a source at $z = 9$ as measured from the lens models are $42''$ and $43''$ for SPT-CL J2325−4111 and SPT-CL J0049−2440, respectively.

- Following Fox et al. (2022), we measured the area magnified by a factor of $\mu \geq 3$ for a source at $z = 9$ (i.e., lensing strength) of $\mathcal{A}^{lens}_{|\mu|\geq 3} = 4.93^{+0.03}_{-0.04}$ arcmin^2, and $\mathcal{A}^{lens}_{|\mu|\geq 3} = 3.64^{+0.14}_{-0.10}$ arcmin^2, for SPT-CL J2325−4111 and SPT-CL J0049−2440, respectively.

- We report on two giant arcs of highly magnified sources in these fields. "J2325 Arc 1" ($z = 1.5790$) is projected $\theta_{arc} = 46''$ north of BCG of SPT-CL J2325−4111, spanning $18''$ in the image plane, with a median magnification of $\mu_{\text{med}} = 10.3$. "J0049 Arc 1" ($z = 3.0220$), projected $\theta_{arc} = 42''$ northeast of the BCG of SPT-CL J0049−2440, spanning $31''$ in the image plane with a median magnification of $\mu_{\text{med}} = 10.9$. Their high distor-

tions indicate promising resolving capabilities for detailed morphological analysis of galaxies at cosmic noon.

We conclude that the lensing power measured at these strong lensing sight-lines promotes SPT-CL J2325−4111 and SPT-CL J0049−2440 to the top tier of strong lensing clusters known today, on par with well-studied clusters such as the Frontier Fields; these clusters have yet untapped potential for follow-up studies of the high-redshift Universe they magnify.

ACKNOWLEDGMENTS

Software: Source Extractor (Bertin & Arnouts 1996); `Lenstool` (Jullo et al. 2007); NOIRLab IRAF v2.18 (Fitzpatrick et al. 2024); AstroDrizzle (Fruchter & et al. 2010); Matlab (Inc. 2022); Astropy (Astropy Collaboration et al. 2013, 2018, 2022) ; MATLAB Astronomy and Astrophysics Toolbox (MAAT; Ofek 2014)

Facilities: HST(ACS, WFC3), Magellan(LDSS3, IMACS, PISCO)

REFERENCES

Acebron, A., Jullo, E., Limousin, M., et al. 2017, MNRAS, 470, 1809

Adamo, A., Bradley, L. D., Vanzella, E., et al. 2024, arXiv e-prints, arXiv:2401.03224

Astropy Collaboration, Robitaille, T. P., Tollerud, E. J., et al. 2013, A&A, 558, A33

Astropy Collaboration, Price-Whelan, A. M., Sipőcz, B. M., et al. 2018, AJ, 156, 123

Astropy Collaboration, Price-Whelan, A. M., Lim, P. L., et al. 2022, ApJ, 935, 167

Atek, H., Richard, J., Kneib, J.-P., et al. 2015, ApJ, 800, 18

Atek, H., Labbé, I., Furtak, L. J., et al. 2024, Nature, 626, 975

Bahé, Y. M. 2021, MNRAS, 505, 1458

Bayliss, M. B., Gladders, M. D., Oguri, M., et al. 2011a, ApJL, 727, L26

Bayliss, M. B., Hennawi, J. F., Gladders, M. D., et al. 2011b, ApJS, 193, 8

Bayliss, M. B., Ruel, J., Stubbs, C. W., et al. 2016, ApJS, 227, 3

Bertin, E., & Arnouts, S. 1996, A&AS, 117, 393

Bezanson, R., Labbe, I., Whitaker, K. E., et al. 2022, arXiv e-prints, arXiv:2212.04026

Bleem, L. E., Stalder, B., de Haan, T., et al. 2015, ApJS, 216, 27

Bleem, L. E., Bocquet, S., Stalder, B., et al. 2020, ApJS, 247, 25

Bocquet, S., Dietrich, J. P., Schrabback, T., et al. 2019, ApJ, 878, 55

Bouwens, R. J., Oesch, P. A., Illingworth, G. D., Ellis, R. S., & Stefanon, M. 2017, ApJ, 843, 129

Cañameras, R., Nesvadba, N. P. H., Guery, D., et al. 2015, A&A, 581, A105

Caminha, G. B., Suyu, S. H., Mercurio, A., et al. 2022, A&A, 666, L9

Cerny, C., Sharon, K., Andrade-Santos, F., et al. 2018, ApJ, 859, 159

Chemerynska, I., Atek, H., Furtak, L. J., et al. 2024, MNRAS, 531, 2615

Claeyssens, A., Adamo, A., Richard, J., et al. 2023, MNRAS, 520, 2180

Coe, D., Salmon, B., Bradac, M., et al. 2019, arXiv e-prints, arXiv:1903.02002

Dahle, H., Gladders, M. D., Sharon, K., Bayliss, M. B., & Rigby, J. R. 2015, ApJ, 813, 67

de La Vieuville, G., Bina, D., Pello, R., et al. 2019, A&A, 628, A3

de Propris, R., Stanford, S. A., Eisenhardt, P. R., Dickinson, M., & Elston, R. 1999, AJ, 118, 719

Diego, J. M., Kaiser, N., Broadhurst, T., et al. 2018, ApJ, 857, 25

Diehl, H. T., Buckley-Geer, E. J., Lindgren, K. A., et al. 2017, ApJS, 232, 15

Dressler, A., Bigelow, B., Hare, T., et al. 2011, PASP, 123, 288

Ebeling, H., Edge, A. C., & Henry, J. P. 2001, ApJ, 553, 668

Elíasdóttir, Á., Limousin, M., Richard, J., et al. 2007, ArXiv e-prints, arXiv:0710.5636

Fischer, T. C., Rigby, J. R., Mahler, G., et al. 2019, arXiv e-prints, arXiv:1903.10403

Fitzpatrick, M., Placco, V., Bolton, A., et al. 2024, arXiv e-prints, arXiv:2401.01982

Fox, C., Mahler, G., Sharon, K., & Remolina González, J. D. 2022, ApJ, 928, 87

Fruchter, A. S., & et al. 2010, in 2010 Space Telescope Science Institute Calibration Workshop, 382–387

Furtak, L. J., Zitrin, A., Weaver, J. R., et al. 2023, MNRAS, 523, 4568

Giocoli, C., Meneghetti, M., Ettori, S., & Moscardini, L. 2012, MNRAS, 426, 1558

Gladders, M. D., & Yee, H. K. C. 2000, AJ, 120, 2148

Gladders, M. D., Allen, S. W., Barrientos, L. F., et al. 2019, Building the SPT-HST Legacy: Imaging Massive Clusters to z=1.5, HST Proposal. Cycle 26, ID. #16017, ,

Golubchik, M., Furtak, L. J., Meena, A. K., & Zitrin, A. 2022, ApJ, 938, 14

Gonzaga, S., Hack, W., Fruchter, A., & Mack, J. 2012, The DrizzlePac Handbook

Grillo, C., Suyu, S. H., Rosati, P., et al. 2015, ApJ, 800, 38

Grillo, C., Rosati, P., Suyu, S. H., et al. 2018, ApJ, 860, 94

Harvey, D., Courbin, F., Kneib, J. P., & McCarthy, I. G. 2017, MNRAS, 472, 1972

Hsiao, T. Y.-Y., Coe, D., Abdurro'uf, et al. 2023, ApJL, 949, L34

Huang, X., Storfer, C., Gu, A., et al. 2021, ApJ, 909, 27

Inc., T. M. 2022, MATLAB version: 9.13.0 (R2022b), Natick, Massachusetts, United States: The MathWorks Inc. https://www.mathworks.com

Jauzac, M., Jullo, E., Kneib, J.-P., et al. 2012, MNRAS, 426, 3369

Jauzac, M., Clément, B., Limousin, M., et al. 2014, MNRAS, 443, 1549

Johnson, T. L., & Sharon, K. 2016, ArXiv e-prints, arXiv:1608.08713

Johnson, T. L., Rigby, J. R., Sharon, K., et al. 2017, ApJL, 843, L21

Jullo, E., Kneib, J.-P., Limousin, M., et al. 2007, New Journal of Physics, 9, 447

Jullo, E., Natarajan, P., Kneib, J.-P., et al. 2010, Science, 329, 924

Kelly, P. L., Diego, J. M., Rodney, S., et al. 2018, Nature Astronomy, 2, 334

Khullar, G., Gozman, K., Lin, J. J., et al. 2021, ApJ, 906, 107

Livermore, R. C., Finkelstein, S. L., & Lotz, J. M. 2017, ApJ, 835, 113

Lotz, J. M., Koekemoer, A., Coe, D., et al. 2017, ApJ, 837, 97

Mahler, G., Natarajan, P., Jauzac, M., & Richard, J. 2023a, MNRAS, 518, 54

Mahler, G., Sharon, K., Fox, C., et al. 2019, ApJ, 873, 96

Mahler, G., Sharon, K., Gladders, M. D., et al. 2020, ApJ, 894, 150

Mahler, G., Jauzac, M., Richard, J., et al. 2023b, ApJ, 945, 49

McDonald, M., Allen, S. W., Bayliss, M., et al. 2017, ApJ, 843, 28

Meneghetti, M., Natarajan, P., Coe, D., et al. 2017, MNRAS, 472, 3177

Meneghetti, M., Davoli, G., Bergamini, P., et al. 2020, Science, 369, 1347

Meneghetti, M., Ragagnin, A., Borgani, S., et al. 2022a, A&A, 668, A188

—. 2022b, A&A, 668, A188

Meneghetti, M., Cui, W., Rasia, E., et al. 2023, A&A, 678, L2

Munari, E., Grillo, C., De Lucia, G., et al. 2016, ApJL, 827, L5

Napier, K., Sharon, K., Dahle, H., et al. 2023, ApJ, 959, 134

Natarajan, P., Chadayammuri, U., Jauzac, M., et al. 2017, MNRAS, 468, 1962

Navarro, J. F., Frenk, C. S., & White, S. D. M. 1996, ApJ, 462, 563

Oemler, A., Clardy, K., Kelson, D., Walth, G., & Villanueva, E. 2017, COSMOS: Carnegie Observatories System for MultiObject Spectroscopy, Astrophysics Source Code Library, record ascl:1705.001, ,

Ofek, E. O. 2014, MAAT: MATLAB Astronomy and Astrophysics Toolbox, Astrophysics Source Code Library, record ascl:1407.005, , , ascl:1407.005

Oke, J. B. 1974, ApJS, 27, 21

Patel, N. R., Jauzac, M., Niemiec, A., et al. 2024, arXiv e-prints, arXiv:2405.04577

Patrício, V., Richard, J., Carton, D., et al. 2018, MNRAS, 477, 18

Postman, M., Coe, D., Benítez, N., et al. 2012, The Astrophysical Journal Supplement Series, 199, 25

Rajan, A. 2010, in WFC3 Data Handbook v. 2, Vol. 2, 2

Remolina Gonzàlez, J. D. 2021, The Concentration-Mass Relation Across Cosmic Time of Strong Lensing Galaxy Clusters, v1.0, Deep Blue, doi:https://dx.doi.org/10.7302/2889. https://deepblue.lib.umich.edu/handle/2027.42/169844

Richard, J., Kneib, J.-P., Ebeling, H., et al. 2011, MNRAS, 414, L31

Rigby, J. R., Vieira, J. D., Phadke, K. A., et al. 2023, arXiv e-prints, arXiv:2312.10465

Rivera-Thorsen, T. E., Dahle, H., Chisholm, J., et al. 2019, Science, 366, 738

Robertson, A. 2021a, MNRAS, 504, L7

—. 2021b, MNRAS, 504, L7

Robertson, A., Harvey, D., Massey, R., et al. 2019, MNRAS, 488, 3646

Ruel, J., Bazin, G., Bayliss, M., et al. 2014, ApJ, 792, 45

Salmon, B., Coe, D., Bradley, L., et al. 2020, ApJ, 889, 189

Schrabback, T., Bocquet, S., Sommer, M., et al. 2021, MNRAS, 505, 3923

Sharon, K., Bayliss, M. B., Dahle, H., et al. 2020, ApJS, 247, 12

Simcoe, R. A., Burgasser, A. J., Schechter, P. L., et al. 2013, PASP, 125, 270

Sirks, E. L., Oman, K. A., Robertson, A., Massey, R., & Frenk, C. 2022, MNRAS, 511, 5927

Smith, G. P., Kneib, J.-P., Smail, I., et al. 2005, MNRAS, 359, 417

Somboonpanyakul, T., McDonald, M., Gaspari, M., Stalder, B., & Stark, A. A. 2021, ApJ, 910, 60

Stalder, B., Stark, A. A., Amato, S. M., et al. 2014, in Proc. SPIE, Vol. 9147, Ground-based and Airborne Instrumentation for Astronomy V, 91473Y

Stark, D. P., Auger, M., Belokurov, V., et al. 2013, MNRAS, 436, 1040

Tam, S.-I., Umetsu, K., & Amara, A. 2022, ApJ, 925, 145

Tokayer, Y. M., Dutra, I., Natarajan, P., et al. 2024, ApJ, 970, 143

Vanderlinde, K., Crawford, T. M., de Haan, T., et al. 2010, ApJ, 722, 1180

Welch, B., Coe, D., Zackrisson, E., et al. 2022, ApJL, 940, L1

Windhorst, R. A., Cohen, S. H., Jansen, R. A., et al. 2023, AJ, 165, 13

Zitrin, A., Seitz, S., Monna, A., et al. 2017, ApJL, 839, L11

APPENDIX

A. SPECTROSCOPIC CATALOGS

We provide in this section spectroscopic catalogs of all the objects in SPT-CL J2325−4111 and SPT-CL J0049−2440 for which spectroscopic redshifts were measured, as described in Section 2.3. For strongly lensed galaxies, see Table 2.

Table 3. List of spectroscopically identified objects in SPT-CL J2325−4111 field of view

ID	R.A. J2000	Decl. J2000	z_{spec}	conf.	Instruments
01401	351.3441640	-41.2209030	0.348900	3	GMOS
01413	351.3497470	-41.1972200	0.160000	3	GMOS
01390	351.3407030	-41.1987940	0.361300	3	GMOS
01368	351.3332750	-41.1982170	0.363900	3	GMOS
01265	351.3085740	-41.2348110	0.363800	3	GMOS
01336	351.3243450	-41.2229620	0.352100	3	GMOS
01218	351.2987820	-41.2038280	0.362400	3	GMOS
01201	351.2953760	-41.1707570	0.192000	3	GMOS
01318	351.3188660	-41.1687860	0.357900	3	GMOS
01241	351.3030290	-41.1961540	0.356700	3	GMOS
01183	351.2921760	-41.2028950	0.350500	3	GMOS
01294	351.3145180	-41.1759540	0.362100	3	GMOS
01348	351.3276450	-41.2226060	0.226000	3	GMOS
01137	351.2802040	-41.1862050	0.489700	3	GMOS
01154	351.2865250	-41.1763750	0.356900	3	GMOS
01121	351.2765190	-41.1656310	0.374400	3	GMOS
01103	351.2699750	-41.1702150	0.356200	3	GMOS
03971	351.2665630	-41.1772930	0.432500	3	GMOS,LDSS3
01057	351.2577900	-41.2204410	0.375700	3	GMOS
01045	351.2523090	-41.2005090	0.367500	3	GMOS
01013	351.2375390	-41.1811040	0.351900	3	GMOS
01027	351.2445480	-41.2360100	0.357100	3	GMOS
01020	351.2410960	-41.2258420	0.432500	3	GMOS
01035	351.2487790	-41.1939490	0.349900	3	GMOS
01394	351.3416100	-41.1752660	0.321000	3	GMOS
01404	351.3447660	-41.2287250	0.356900	3	GMOS
01411	351.3487220	-41.1709890	0.347200	3	GMOS
01372	351.3346820	-41.1703420	0.362000	3	GMOS
01270	351.3091410	-41.2274320	0.355300	3	GMOS
01340	351.3247990	-41.2043660	0.362200	3	GMOS
01197	351.2954430	-41.1902700	0.491300	3	GMOS

Table 3 *continued*

Table 3 *(continued)*

ID	R.A. J2000	Decl. J2000	z_{spec}	conf.	Instruments
01312	351.3177880	-41.2039130	0.356600	3	GMOS,LDSS3
01225	351.3000300	-41.1990380	0.353900	3	GMOS
01245	351.3043020	-41.1951820	0.350500	3	GMOS
01290	351.3142180	-41.2351900	0.312900	3	GMOS
01349	351.3278620	-41.2207260	0.348400	3	GMOS
01329	351.3214490	-41.1846350	0.313200	3	GMOS
01148	351.2842540	-41.1864490	0.366400	3	GMOS
01135	351.2801310	-41.2032250	0.367700	3	GMOS
01094	351.2683210	-41.1910510	0.321900	3	GMOS,IMACS
01164	351.2882280	-41.2252490	0.348700	3	GMOS
01107	351.2721890	-41.1771660	0.321400	3	GMOS
01070	351.2609010	-41.1530830	0.359500	3	GMOS
01054	351.2563260	-41.2219040	0.374600	3	GMOS
01046	351.2526510	-41.1843500	0.335100	3	GMOS
04869	351.2485840	-41.1571180	0.702000	3	GMOS
01011	351.2369250	-41.1530090	0.220300	3	GMOS
1000000	351.3035706	-41.2089879	0.5977	3	LDSS3
1000002	351.3087817	-41.2094812	1.2530	3	LDSS3
1000004	351.2916434	-41.1847361	0.4605	3	LDSS3
1000006	351.3056850	-41.1922042	0.6584	3	LDSS3
1000007	351.3188893	-41.2330244	0.3609	3	LDSS3
1000008	351.3084807	-41.1828173	1.7742	3	LDSS3
1000009	351.3062829	-41.1834300	1.2476	3	LDSS3
1000010	351.3108177	-41.1830207	0.4077	3	LDSS3
1000011	351.3292737	-41.1694328	0.3128	3	LDSS3
1000012	351.3298597	-41.1746109	0.3548	3	LDSS3
1000013	351.3440608	-41.1963206	0.3616	3	LDSS3,IMACS
1000014	351.3106927	-41.1703992	0.3591	3	LDSS3
1000015	351.3129579	-41.1807395	0.3034	3	LDSS3
1000016	351.3359554	-41.1846179	0.3488	3	LDSS3
1000017	351.3143582	-41.1692656	0.3522	3	LDSS3
1000018	351.3115126	-41.1750614	0.1728	3	LDSS3
1000019	351.3026622	-41.2254834	0.3493	3	LDSS3
1000020	351.2815989	-41.2078578	0.3585	3	LDSS3
1000021	351.2850689	-41.2131094	0.3587	3	LDSS3
1000022	351.2928224	-41.2258305	0.4028	3	LDSS3
1000023	351.2831678	-41.2190378	0.3634	3	LDSS3
1000024	351.2918273	-41.2324123	0.4881	3	LDSS3
1000025	351.2907580	-41.2348826	0.3635	3	LDSS3
1000026	351.2868297	-41.2463011	0.3603	3	LDSS3,IMACS
1000027	351.2827486	-41.2013488	0.3552	3	LDSS3

Table 3 *continued*

Mahler et al.

Table 3 *(continued)*

ID	R.A. J2000	Decl. J2000	z_{spec}	conf.	Instruments
1000028	351.2940010	-41.2501492	0.3383	3	LDSS3
1000029	351.2756630	-41.2396156	0.6814	3	LDSS3
1000030	351.2530784	-41.2350867	0.5790	3	LDSS3
1000031	351.2689117	-41.2478494	0.4635	3	LDSS3
1000032	351.2955916	-41.2465336	0.3617	3	LDSS3
1000033	351.2653446	-41.2353025	0.3683	3	LDSS3
1000034	351.3481379	-41.1745702	0.3616	3	LDSS3
1000035	351.3354588	-41.1733367	0.3398	3	LDSS3
1000036	351.3690074	-41.1931554	0.3566	3	LDSS3,IMACS
1000037	351.3040458	-41.2116733	1.3211	3	LDSS3
1000037	351.3030531	-41.2119615	0.9083	3	LDSS3
1000000	351.2934811	-41.2082503	0.2542	3	LDSS3
1000001	351.2919703	-41.2070080	0.2544	3	LDSS3
1000002	351.3118027	-41.2034595	2.1890	3	LDSS3
1000003	351.3108949	-41.2000035	0.5609	3	LDSS3
1000004	351.2958046	-41.2101419	0.1145	3	LDSS3
1000005	351.3077958	-41.2157158	1.2870	3	LDSS3
1000006	351.3188007	-41.2043415	1.5811	3	LDSS3
1000006	351.3196598	-41.2045284	1.2548	3	LDSS3
1000008	351.2966835	-41.1869120	0.5790	3	LDSS3
1000009	351.2997517	-41.2165675	0.8437	3	LDSS3
1000010	351.3251136	-41.2092826	0.3551	3	LDSS3
1000011	351.3402885	-41.2132521	0.3481	3	LDSS3
1000012	351.3207483	-41.2384890	0.3563	3	LDSS3
1000013	351.3245493	-41.2030424	0.3429	3	LDSS3
1000014	351.3172530	-41.2319393	0.3671	3	LDSS3
1000015	351.3417345	-41.2322558	0.3668	3	LDSS3
1000016	351.3478817	-41.2339794	0.3597	3	LDSS3
1000017	351.3395725	-41.2305706	0.3503	3	LDSS3
1000018	351.3634325	-41.2211889	0.3598	3	LDSS3
1000019	351.3607681	-41.2200194	0.3522	3	LDSS3
1000020	351.3655344	-41.2040346	0.3549	3	LDSS3
1000021	351.2783992	-41.1973868	0.3464	3	LDSS3
1000022	351.2794197	-41.2123900	0.3588	3	LDSS3
1000023	351.2778861	-41.1858110	0.4889	3	LDSS3
1000024	351.2758972	-41.1709807	0.3597	3	LDSS3
1000025	351.2617899	-41.1796658	0.3457	3	LDSS3
1000026	351.2620483	-41.1927381	0.3488	3	LDSS3
1000027	351.2634913	-41.2052930	0.3748	3	LDSS3
1000028	351.2786270	-41.1887002	0.3434	3	LDSS3
1000029	351.3550048	-41.2530103	0.3568	3	LDSS3

Table 3 *continued*

Table 3 *(continued)*

ID	R.A. J2000	Decl. J2000	z_{spec}	conf.	Instruments
1000030	351.3597963	-41.2380938	0.5543	3	LDSS3
1000031	351.3571694	-41.2087321	0.1367	3	LDSS3
1000032	351.3201482	-41.2467900	0.3544	3	LDSS3
1000033	351.2657143	-41.1523966	0.3470	3	LDSS3,IMACS
1000034	351.2628524	-41.1636893	0.6594	3	LDSS3
1000035	351.2716906	-41.1533293	0.4840	3	LDSS3
1000037	351.2543306	-41.1665713	0.3458	3	LDSS3
1000038	351.2598936	-41.1506836	0.5102	3	LDSS3
1000039	351.2699605	-41.2269533	0.3551	3	LDSS3
1000040	351.3223366	-41.2291830	0.3668	3	LDSS3
1000042	351.2971077	-41.2142311	1.2487	2	LDSS3,IMACS
1000043	351.3197344	-41.1970816	0.3488	3	LDSS3
1	351.3307531	-41.1975129	0.1875	3	IMACS
3	351.3087164	-41.1913390	1.3428	2	IMACS
4	351.3200478	-41.1920123	1.2885	1	IMACS
6	351.3161614	-41.1916622	0.4895	3	IMACS
6	351.3145867	-41.1918808	0.3907	3	IMACS
7	351.3387738	-41.1982031	0.0472	3	IMACS
8	351.0908000	-41.3856000	0.4153	2	IMACS
9	351.1680792	-41.3749842	0.5778	3	IMACS
10	351.0430226	-41.3757393	0.5786	3	IMACS
11	351.2371158	-41.3606047	0.4233	3	IMACS
12	351.3294233	-41.3514408	0.3733	3	IMACS
13	351.1325777	-41.3470125	0.6027	3	IMACS
14	351.2191606	-41.3444107	0.5488	1	IMACS
15	350.9874171	-41.3408072	0.6919	3	IMACS
16	351.0768385	-41.3258616	0.3180	1	IMACS
17	351.2389775	-41.3234121	0.3647	2	IMACS
18	351.2486345	-41.3151546	0.3594	3	IMACS
19	351.2426654	-41.3158980	0.4471	2	IMACS
20	350.9797792	-41.3149806	0.2994	3	IMACS
21	351.1704507	-41.3095811	0.6399	3	IMACS
22	351.1442806	-41.3089506	0.5796	3	IMACS
23	351.4607480	-41.3064505	0.3736	3	IMACS
24	351.2438396	-41.2984098	0.3648	3	IMACS
25	351.5309839	-41.2948694	0.3603	3	IMACS
26	350.9971620	-41.2896735	0.3008	3	IMACS
27	351.5024523	-41.2944313	0.5597	3	IMACS
28	351.3999741	-41.2879101	0.3593	3	IMACS
29	350.9866289	-41.2834291	0.3169	3	IMACS
30	351.1946338	-41.2852857	0.3603	3	IMACS

Table 3 *continued*

Table 3 *(continued)*

ID	R.A. J2000	Decl. J2000	z_{spec}	conf.	Instruments
31	351.5030315	-41.2845684	0.5808	1	IMACS
32	351.1798852	-41.2834147	0.3247	3	IMACS
33	351.2698396	-41.2808630	0.3561	3	IMACS
34	351.2997460	-41.2781853	0.3486	3	IMACS
35	351.0889352	-41.2772592	0.4247	3	IMACS
36	351.4587165	-41.2757527	0.3574	3	IMACS
37	351.4353233	-41.2757739	0.3539	3	IMACS
38	350.9299940	-41.2689700	0.3143	3	IMACS
39	351.2705655	-41.2716035	0.3097	3	IMACS
40	351.5135874	-41.2694621	0.5815	3	IMACS
41	351.4631121	-41.2631035	0.3757	3	IMACS
42	351.4658950	-41.2616775	0.3586	3	IMACS
43	351.3125910	-41.2569106	0.3655	3	IMACS
44	351.1596829	-41.2537828	0.4932	3	IMACS
45	351.5377888	-41.2518169	0.4201	3	IMACS
46	351.4336385	-41.2458311	0.3479	3	IMACS
46	351.4343508	-41.2456887	0.3492	2	IMACS
47	351.4390198	-41.2482455	0.3727	3	IMACS
48	350.9284946	-41.2431137	0.6768	3	IMACS
49	351.2477438	-41.2423766	0.3553	3	IMACS
50	351.5111342	-41.2420319	0.0	3	IMACS
50	351.5119582	-41.2417901	0.2711	1	IMACS
51	351.2195562	-41.2384889	0.3649	3	IMACS
52	351.1296429	-41.2374986	0.3747	3	IMACS
54	351.5199697	-41.2356103	0.3756	3	IMACS
55	351.3677532	-41.2340216	0.3531	3	IMACS
56	351.0694769	-41.2290305	0.3001	2	IMACS
57	350.9897473	-41.2280795	0.4462	3	IMACS
58	351.3798623	-41.2272595	0.3522	3	IMACS
59	351.0441194	-41.2239418	0.3178	3	IMACS
60	351.1176601	-41.2235394	0.4068	3	IMACS
61	351.4847129	-41.2227832	0.3208	3	IMACS
62	351.0360547	-41.2219622	0.0	3	IMACS
63	351.5055554	-41.2184035	0.3752	3	IMACS
64	351.2240318	-41.2007740	0.3305	2	IMACS
67	351.1644843	-41.1949432	0.6588	3	IMACS
68	350.9375484	-41.1945333	0.4137	3	IMACS
70	351.4827107	-41.1917357	0.4659	3	IMACS
71	351.2136769	-41.1890435	0.3605	2	IMACS
72	351.1140503	-41.1849005	0.2999	2	IMACS
73	351.3939791	-41.1787078	0.3777	3	IMACS

Table 3 *continued*

Table 3 *(continued)*

ID	R.A. J2000	Decl. J2000	z_{spec}	conf.	Instruments
74	350.9263901	-41.1795695	0.4174	3	IMACS
75	351.4277158	-41.1742006	0.3748	3	IMACS
76	351.3794157	-41.1741300	0.4108	3	IMACS
77	350.9935886	-41.1697505	0.4160	3	IMACS
78	350.9680695	-41.1679272	0.3124	3	IMACS
79	351.1282096	-41.1689561	0.3681	2	IMACS
80	351.0685270	-41.1668891	0.5927	3	IMACS
81	351.4073441	-41.1579148	0.3597	3	IMACS
82	351.1513607	-41.1565862	0.3667	3	IMACS
82	351.1517969	-41.1563888	0.4063	1	IMACS
83	351.2608321	-41.1583439	0.3625	3	IMACS
84	351.4254882	-41.1566662	0.3553	3	IMACS
85	351.1652313	-41.1546266	0.2826	1	IMACS
86	350.9918061	-41.1505843	0.3572	3	IMACS
87	351.1599352	-41.1516310	0.3515	1	IMACS
88	351.1360050	-41.1470098	0.3708	3	IMACS
89	351.4205442	-41.1382882	0.3729	3	IMACS
90	351.3324299	-41.1383155	0.3583	3	IMACS
91	351.1183336	-41.1359333	0.3021	3	IMACS
92	351.3531781	-41.1347803	0.4128	3	IMACS
93	351.4219075	-41.1241488	0.3744	1	IMACS
94	351.2055221	-41.1237165	0.3499	2	IMACS
95	351.3152562	-41.1132695	0.3563	3	IMACS
96	351.3813927	-41.0953665	0.4896	3	IMACS
97	351.3453414	-41.0850716	0.4351	3	IMACS
98	351.4456225	-41.0799043	0.2407	1	IMACS
99	351.3581700	-41.0769170	0.3112	3	IMACS
100	351.4312135	-41.0736623	0.4108	3	IMACS
101	351.4091380	-41.0565935	0.4109	3	IMACS

NOTE—Spectroscopic redshifts measured in SPT-CL J2325−4111 from Gemini, Magellan/LDSS3, and Magellan/IMACS. See Section 2.3 for details of the spectroscopy analysis. Strongly lensed galaxies are tabulated in Table 2.

Table 4. List of spectroscopically identified objects in SPT-CL J0049−2440 field of view

ID	R.A. J2000	Decl. J2000	z_{spec}	conf.	Instruments
030	12.2958676	-24.6396331	0.3445	1	LDSS3
025	12.2976676	-24.6445438	0.2752	2	LDSS3
024	12.2947339	-24.6482300	0.5279	3	LDSS3
027	12.3155564	-24.6437909	0.5318	3	LDSS3
023	12.2940359	-24.6542052	0.2492	3	LDSS3
026	12.3073222	-24.6526637	0.3426	3	LDSS3
028	12.3072829	-24.6551361	0.3448	3	LDSS3
022	12.2909294	-24.6640596	0.4341	3	LDSS3
006	12.2876854	-24.6674970	0.4440	1	LDSS3
010	12.2893727	-24.6700378	0.0	1	LDSS3
011	12.2751750	-24.6766800	0.9398	3	LDSS3
004	12.3026499	-24.6699485	0.746	1	LDSS3
002	12.2849216	-24.6888735	1.0302	2	LDSS3
001	12.2888840	-24.6913042	0.4299	1	LDSS3
009	12.2985897	-24.6906095	0.5355	3	LDSS3
005	12.3041248	-24.6907131	1.72	1	LDSS3
012	12.3042900	-24.6931631	0.5293	3	LDSS3
013	12.2957763	-24.6986553	0.5321	3	LDSS3
014	12.2821687	-24.7062031	0.5265	3	LDSS3
015	12.2867523	-24.7068513	0.5185	2	LDSS3
034	12.2776163	-24.7128064	0.3572	3	LDSS3
017-A	12.3229906	-24.7002583	0.3141	3	LDSS3
017-B	12.3227230	-24.6997445	0.2482	1	LDSS3
016	12.3205370	-24.7033231	0.4047	3	LDSS3
018	12.2758188	-24.7225908	0.1910	2	LDSS3
020	12.3018904	-24.7172519	0.9065	3	LDSS3
019	12.2965644	-24.7212467	0.437	1	LDSS3
021	12.3004454	-24.7249998	0.5247	3	LDSS3
033	12.3159975	-24.7222300	0.5234	2	LDSS3
032	12.3054420	-24.7283286	0.4038	1	LDSS3

NOTE—Spectroscopic redshifts measured in SPT-CL J0049−2440 from Magellan/LDSS3. See Section 2.3 for details of the spectroscopy analysis. Strongly lensed galaxies are tabulated in Table 2. 017-A and 017-B are two different galaxy detection from the same slit, ID017.

B. SPT-CL J0512−3848

A third cluster, SPT-CL J0512−3848, was flagged as a promising strong lens candidate as part of our HST program to identify the next generation of extraordinary cluster lenses (GO-15937; PI: G. Mahler). The cluster was cataloged in Bleem et al. (2020) with significance $\xi = 7.54$, $z = 0.326$, and $M_{500c} = 6.07^{+0.87}_{-0.88} \times 10^{14} h_{70}^{-1} \mathrm{M}_\odot$. Ground based optical
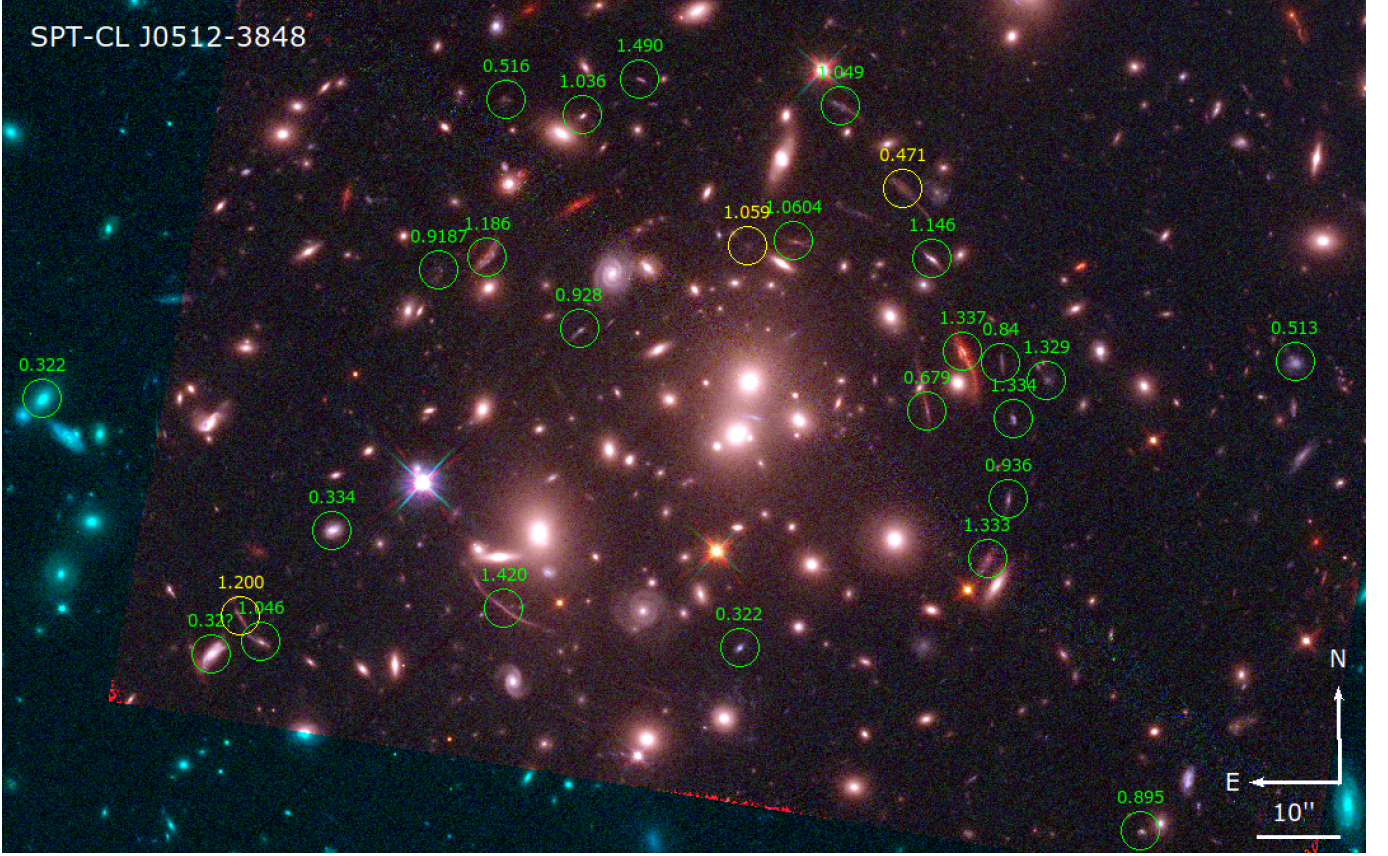
Figure 8. Composite color images of the field of SPT-CL J0512−3848, from HST imaging in WFC3IR/F140W (red), ACS/F814W (green), and ACS/F606W (blue). Circles labeled the spectroscopic redshift identified. Green circles correspond to high confidence identification while yellow circles mark tentative redshift identification. The full list of identification is listed in Table 5.

imaging with Magellan/PISCO revealed promising arc-like features (see Figure 8 in Bleem et al. 2020). Despite the preliminary evidence, the combined analysis of HST morphology and extensive LDSS3 spectroscopy indicated that most of the arc-like features are high-flexure singly imaged lensed galaxies at $z < 2$. While the cluster is likely a strong lens, there is not sufficient evidence for a robust lens model. In particular, we do not identify secure cluster-wide multiply-imaged systems. The field was observed with multi-object slit masks on 2017 Jan 1, 2017 Jan 30, 2017 Sep 2, 2018 Jan 9-10, and 2020 Jan 23 (Remolina Gonzàlez 2021, Table D.1). Data reduction and spectroscopic analysis were as described in Section 2.3. In this appendix, we provide the LDSS3 spectroscopic redshifts we obtained in this field, to facilitate possible future investigations of this line of sight by the community. Galaxies with spectroscopic redshifts at the core of SPT-CL J0512−3848 are labeled in Figure 8, overplotted on the HST imaging from GO-15937. Table 5 presents the spectroscopic redshifts of all the objects in the field observed using Magellan/LDSS3 instruments as part of the follow-up of SPT clusters, out to $\sim 2.5'$ from the BCG.

Table 5. List of spectroscopically identified objects in SPT-CL J0512−3848 field of view

ID	R.A. J2000	Decl. J2000	z_{spec}	conf.	Instruments
1	78.2523417	-38.7977722	1.420	3	LDSS3

Table 5 *continued*

Mahler et al.

Table 5 *(continued)*

ID	R.A. J2000	Decl. J2000	z_{spec}	conf.	Instruments
2	78.2634083	-38.7980306	1.200	2	LDSS3
3	78.2550625	-38.7866944	0.9187	3	LDSS3
4	78.2330458	-38.7893667	1.337	3	LDSS3
5	78.2295042	-38.7903139	1.329	3	LDSS3
6	78.2595542	-38.7952194	0.334	3	LDSS3
7	78.2625458	-38.7988722	1.046	3	LDSS3
8	78.2646458	-38.7992667	0.32	2	LDSS3
9	78.2530417	-38.7862778	1.186	3	LDSS3
10	78.2343458	-38.7863167	1.146	3	LDSS3
11	78.2421125	-38.7858972	1.059	2	LDSS3
12	78.2355625	-38.7840167	0.471	2	LDSS3
13	78.2381708	-38.7813083	1.049	3	LDSS3
14	78.2490208	-38.7816333	1.036	3	LDSS3
15	78.2522458	-38.7811111	0.516	3	LDSS3
16	78.2466083	-38.7804389	1.490	3	LDSS3
17	78.2636375	-38.7742222	0.872	3	LDSS3
18	78.2345424	-38.7913338	0.679	3	LDSS3
19	78.2309167	-38.7915861	1.334	3	LDSS3
20	78.2320000	-38.7961528	1.333	3	LDSS3
21	78.2424292	-38.7990694	0.322	3	LDSS3
22	78.2190708	-38.7897111	0.513	3	LDSS3
23	78.2145583	-38.7762639	0.324	3	LDSS3
24	78.2255500	-38.8050750	0.895	3	LDSS3
25	78.2218708	-38.8072361	0.444	3	LDSS3
26	78.2558125	-38.8102667	1.607	2	LDSS3
27	78.2717333	-38.7909111	0.322	3	LDSS3
28	78.2491579	-38.7886275	0.928	3	LDSS3
29	78.2401483	-38.7857283	1.0604	3	LDSS3
30	78.2311376	-38.7942000	0.936	3	LDSS3
31	78.2314275	-38.7897544	0.84	3	LDSS3

Note—Spectroscopic redshifts measured in SPT-CL J0512−3848 from Magellan/LDSS3. See Section 2.3 for details of the spectroscopy analysis.

C. LENSING CANDIDATES

In this section we provide a zoom-in view of the multiple images identified in this work and used as lens modeling constraints, in Figure 9. See Table 2 for coordinates, Figure 1 and Figure 2 for the full field of view of each cluster with arcs labeled. Section 3.2 describes the identification.

SPT-CLJ2325−4111
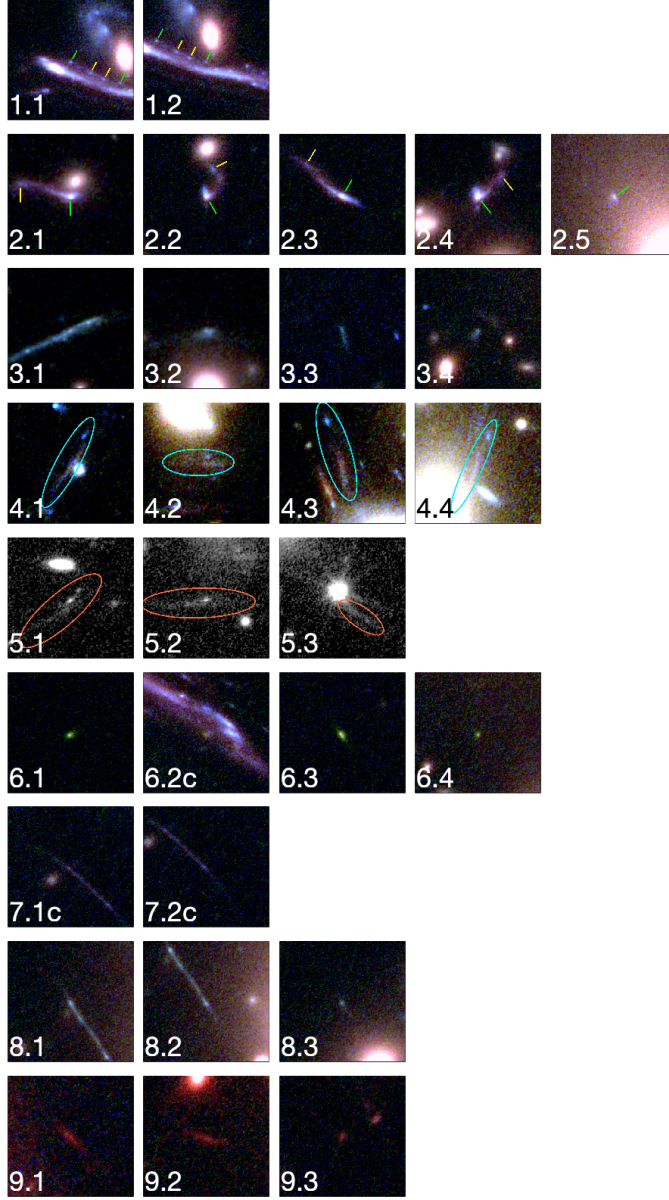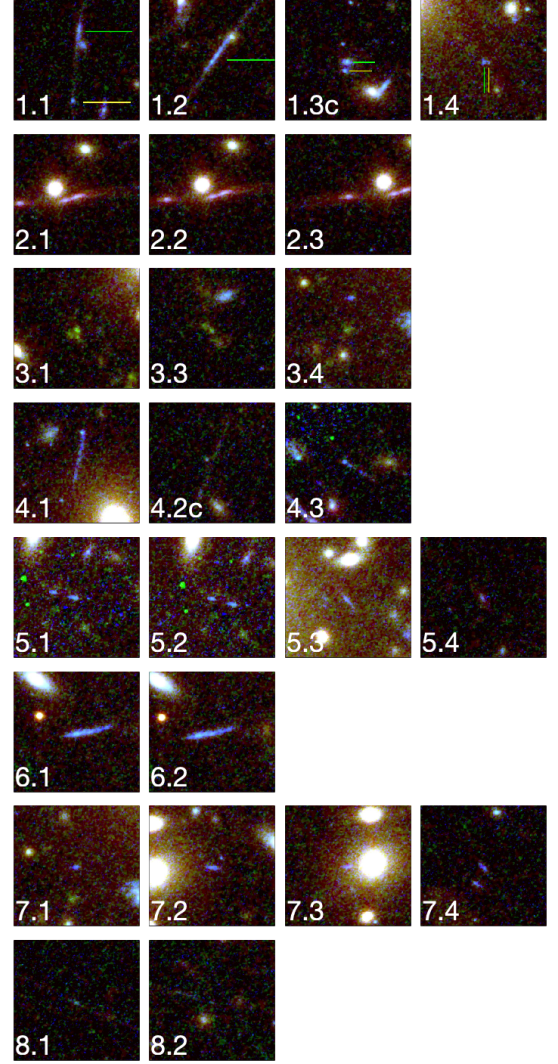
SPT-CLJ0049-2440

Figure 9. Zoom-in on the multiple images of lensed galaxies in SPT-CL J2325−4111 (left) and SPT-CL J0049−2440 (right). Each square is $3\rlap{.}''0 \times 3\rlap{.}''0$ field of view, with the exception of images of sources 4 and 5 in SPT-CL J2325−4111, which are $4\rlap{.}''0 \times 4\rlap{.}''0$. Most images are centered on the clump that was identified as constraint. In SPT-CL J2325−4111 source 4, the blue emission knot at the north of each arc was used as the constraint. The color rendition is the same as Figure 1 and Figure 2. For SPT-CL J2325−4111 source 5, we show only F814W in grayscale, since image 5.3 of the source is affected by diffraction spikes of a nearby star in the other bands. Green and yellow ticks mark the first and second clumps, respectively, in systems where multiple clumps were used as constraints.